Seasonal changes in the middle atmosphere of Titan from Cassini/CIRS observations: Temperature and trace species abundance profiles from 2004 to 2017

Christophe Mathé [a],*, Sandrine Vinatier [a], Bruno Bézard [a], Sébastien Lebonnois [b], Nicolas Gorius [c], Donald E. Jennings [c], Andrei Mamoutkine [d], Ever Guandique [e], Jan Vatant d'Ollone [b]

[a] LESIA, Observatoire de Paris, Université PSL, CNRS, Sorbonne Université, Université de Paris, 5 place Jules Janssen, Meudon 92195, France
[b] Laboratoire de Météorologie Dynamique, Sorbonne Université, ENS, Université PSL, Ecole Polytechnique, Université Paris-Saclay, CNRS, France
[c] NASA/Goddard Space Flight Center, Code 693, Greenbelt, MD 20771, USA
[d] Department of Astronomy, University of Maryland, College Park, MD 20742, USA
[e] ADNET Systems, Inc., Bethesda, MD 20817, USA

ARTICLE INFO

ABSTRACT

The Cassini/Composite InfraRed Spectrometer (CIRS) instrument has been observing the middle atmosphere of Titan over almost half a Saturnian year. We used the CIRS dataset processed through the up-to-date calibration pipeline to characterize seasonal changes of temperature and abundance profiles in the middle atmosphere of Titan, from mid-northern winter to early northern summer all around the satellite. We used limb spectra from 590 to 1500 cm^{-1} at 0.5-cm^{-1} spectral resolution, which allows us to probe different altitudes. We averaged the limb spectra recorded during each flyby on a fixed altitude grid to increase the signal-to-noise ratio. These thermal infrared data were analyzed by means of a radiative transfer code coupled with an inversion algorithm, in order to retrieve vertical temperature and abundance profiles. These profiles cover an altitude range of approximately 100 to 600 km, at 10- or 40-km vertical resolution (depending on the observation). Strong changes in temperature and composition occur in both polar regions where a vortex is in place during the winter. At this season, we observe a global enrichment in photochemical compounds in the mesosphere and stratosphere and a hot stratopause located around 0.01 mbar, both linked to downwelling in a pole-to-pole circulation cell. After the northern spring equinox, between December 2009 and April 2010, a stronger enhancement of photochemical compounds occurred at the north pole above the 0.01-mbar region, likely due to combined photochemical and dynamical effects. During the southern autumn in 2015, above the South pole, we also observed a strong enrichment in photochemical compounds that contributed to the cooling of the stratosphere above 0.2 mbar (~300 km). Close to the northern spring equinox, in December 2009, the thermal profile at 74°N exhibits an oscillation that we interpret in terms of an inertia-gravity wave.

1. Introduction

The Cassini spacecraft has been exploring the Saturnian system between July 2004 and September 2017. During almost half a Saturnian year, it performed 127 close flybys of Titan. The stratosphere and mesosphere of Titan are mainly composed of N_2 (98.4%) and CH_4 (1.5%) with traces of dihydrogen, hydrocarbons, nitriles and oxygen compounds (Bézard et al., 2014). The two main compounds, N_2 and CH_4, are dissociated by the ultraviolet solar flux and by electrons from Saturn's magnetosphere, which leads to the formation of photochemical compounds and aerosols through complex pathways. One-dimensional photochemical models, coupling neutral and ion chemistry together with vertical eddy transport and condensation, have been developed by different groups (see, e.g. Dobrijevic et al., 2016; Krasnopolsky, 2014; Loison et al., 2015; Vuitton et al., 2019, for the most recent ones). Saturn's obliquity induces strong seasonal changes in Titan's atmosphere.

In winter/summer seasons, general circulation models (GCM) predict a pole-to-pole circulation cell in the middle atmosphere with the ascending branch located at the summer pole and the descending branch at the winter pole (Lebonnois et al., 2012; Lora et al., 2015; Newman et al., 2011). A polar vortex, present during winter, vanishes in early spring. Around the equinoxes, GCMs predict the presence of two equator-to-pole circulation cells in the middle atmosphere, with an ascending branch at low latitudes and descending branches at both poles (Lebonnois et al., 2012; Lora et al., 2015; Newman et al., 2011). The descending branches of these pole-to-pole or equator-to-pole circulation cells enrich in photochemical compounds and adiabatically heats the mesosphere at high latitudes.

Various analyses of spectra recorded by the Cassini/CIRS (Composite InfraRed Spectrometer) have highlighted seasonal changes in temperature and abundance profiles (for the most recent publications, see e.g., Vinatier et al., 2015; Teanby et al., 2017; Sylvestre et al., 2018; Coustenis et al., 2019; Teanby et al., 2019). In particular, thermal and abundance profiles in the middle atmosphere (between 20 and 0.001 mbar) have been monitored by Vinatier et al. (2015) from 2006 to 2013. In the northern polar region, the temperatures in the pressure range 0.4 –0.002 mbar observed during the winter, from 2006 to 2008, were higher than in the 2010–2011 period. This probably results from the adiabatic heating provided by the descending branch of the pole-to-pole circulation cell which is stronger during winter (Achterberg et al., 2011). Still during winter, the northern polar region was enriched in photochemical compounds compared to the equatorial region, from the lower stratosphere (Coustenis et al., 2019; Sylvestre et al., 2018; Teanby et al., 2019) to the mesosphere (Vinatier et al., 2015). Then, from 2009 to 2010, shortly after northern spring equinox (August 2009), the northern polar region exhibited a stronger enrichment in photochemical compounds above 0.1 mbar compared to winter. This feature may result from a combination of dynamics and chemistry, in which the solar flux reappearing after the polar night locally reactivates the photochemical production of most species that are then transported downwards by the equator-to-pole circulation cell (Vinatier et al., 2015). This study also suggests that both equator-to-pole cells coexisted from at last January 2010 to at least June 2010. In the southern polar region, a mesospheric hot spot around 0.01 mbar ($\sim$400 km) appeared between 2010 and 2011, likely due to the increasing strength of the adiabatic heating provided by the descending air branch (Teanby et al., 2017, 2012; Vinatier et al., 2015). During northern spring, between 2012 and early 2015, Teanby et al. (2017) observed a cold mesosphere near the south pole, which they attributed to a radiative effect linked to the mesospheric enrichment in photochemical compounds inside the polar vortex. This trace gas enrichment, likely resulting from downwelling in the pole-to-pole circulation cell, was also observed in the lower stratosphere at 15 mbar (Sylvestre et al., 2018). From 2015 onwards, the mesosphere near the south pole warmed up, probably due to the increase of the subsidence velocity in the descending branch of the circulation cell (Teanby et al., 2017).

Vinatier et al. (2015) studied the seasonal changes between October 2006 and May 2012 using CIRS mid-IR limb spectra acquired at the highest available spectral resolution (0.5 cm^{-1}). These authors inferred thermal and abundance profiles (C_2H_2, C_2H_4, C_2H_6, C_3H_8, C_3H_4, C_4H_2, C_6H_6, CO_2, HCN, HC_3N) at altitudes between 100 and 550 km. In this study, we extended the analysis of the 0.5 cm^{-1} mid-IR limb spectra to the whole dataset acquired during the entire Cassini mission between 2004 and 2017, and using a new methodology, we were able to probe from 100 to around 650 km altitude. This study is complementary to the work of Coustenis et al. (2019) who analyzed nadir CIRS mid-IR spectra at 0.5 cm^{-1} spectral resolution between 2010 and 2017, probing deeper altitude levels (between 20 mbar and 0.05 mbar, depending on the molecule, i.e. $\sim$80 and 315 km). Teanby et al. (2019) analyzed mid-IR CIRS nadir spectra acquired with a lower spectral resolution of 2.5 cm^{-1} between 2004 and 2017, probing similar altitude levels (5 to 0.1 mbar, $\sim$115 to 280 km) than Coustenis et al. (2019). Using CIRS far-

IR nadir spectra, Sylvestre et al. (2018) monitored seasonal changes in C_4H_2, C_3H_4 and C_2N_2 abundance profiles at 15 mbar ($\sim$85 km), which is deeper than levels probed in the mid-IR spectral range.

We present here an analysis of the whole set of Cassini/CIRS limb spectra recorded at 0.5-cm^{-1} resolution during 56 of the 127 Titan fly-bys. Our goal is to document the seasonal changes in temperature and composition that take place in the stratosphere and lower mesosphere, at all covered latitudes (poles, mid-latitudes and equator), and during the entire Cassini mission from 2004 to 2017. Data selection is described in Section 2 and the methodology used to retrieve the temperature and gas abundance profiles is detailed in Section 3. Thermal and abundance profiles of C_2H_2, C_2H_4, C_2H_6, C_3H_4, C_3H_8, C_4H_2, C_6H_6, HCN, HC_3N and CO_2 are shown in Section 4. The results are discussed in Section 5 and a brief conclusion is presented in Section 6.

2. Observations

The CIRS spectrometer was composed of three focal planes (FP) covering the 10–1500 cm^{-1} wavenumber range: FP1 (10 to 600 cm^{-1}), FP3 (580 to 1100 cm^{-1}) and FP4 (1050 to 1500 cm^{-1}). We used both FP3 and FP4, which are each composed of an array of 1 × 10 pixels. This linear shape is relevant for limb viewing geometry, as the line-of-sight of each pixel traverses the atmosphere down to a given tangent height, which varies from the surface to about 700 km. However, even for low tangent heights, limb spectra cannot probe deeper than a pressure level of $\sim$ 5–6 mbar ($\sim$115 km), due to the large increase of the opacity in the molecular emission bands around this pressure level. Each pixel has a 0.27×0.27 mrad^2 field-of-view corresponding to a vertical resolution varying from 10 to 40 km (comparable to a pressure scale height), depending on the distance of the spacecraft to Titan during the flyby. More details on the CIRS instrument are given in Kunde et al. (1996), Flasar et al. (2004) and Jennings et al. (2017), and more details on the different types of observations are given in Nixon et al. (2019).

We used the CIRS "global calibration" database described in Jennings et al. (2017). We selected limb spectra with a spectral resolution of 0.5 cm^{-1} for which gas molecular emission bands are well separated. Spectral selections cover the entire Cassini mission, from the northern winter in December 2004 to the early northern summer in September 2017, and pole-to-pole latitudes. Characteristics of the observations that we used are listed in Table 1 (Appendix A).

In order to increase the signal-to-noise ratio, we averaged all available limb spectra acquired during a given observation sequence and having close enough tangent heights (see Appendix B for more details on our averaging method). For some flybys (Tb, T06, T16, T28, T59, T84, T103, T120), we complemented the limb spectra with an average of nadir spectra to extend the information available from the retrievals to lower altitudes.

For a couple of observations, limb spectra with the highest tangent heights presented negative continua in the 1075–1200 cm^{-1} spectral range due to calibration problems. We developed a procedure that corrects this negative continuum, and allowed us to determine the error due to this effect on temperature and abundance profile retrievals (see Appendix C).

3. Retrieval methodology

CIRS acquired spectra of the thermal emission of Titan's atmosphere. Molecular gases emit through their rotation and ro-vibration bands, the intensity of which depends on both temperature and gas mixing ratio profiles. The continuum emission is due to the haze opacity and collision-induced absorption of N_2-N_2, N_2-H_2, N_2-CH_4 and CH_4-CH_4.

To infer thermal and molecular mixing ratio profiles from CIRS observations, we proceeded as follows: first, we retrieved the thermal profile by fitting the ν_4 CH_4 band at 1306 cm^{-1}, assuming a constant methane mixing ratio of 1.48%, as measured *in situ* by the GCMS instrument (Niemann et al., 2010). The impact of this hypothesis on the

retrieved thermal profiles is discussed in Appendix D. We also assumed that temperature profiles did not vary with longitude as suggested by Flasar et al. (2005). Secondly, molecular gas mixing ratio profiles were inferred using the retrieved thermal profile. Each profile retrieval have been performed using a correlation length equal to the vertical resolution of the limb spectra dataset for a given observation (see Table 1).

Retrievals were performed using a line-by-line radiative transfer code coupled with a constrained linear inversion algorithm, described in Conrath et al. (1998) and Vinatier et al. (2015).

References for the spectroscopic data used here can be found in Vinatier et al. (2010a, 2015), except for the HCN, HC^{15}N and H^{13}CN spectroscopic files that we updated from GEISA (Jacquinet-Husson et al., 2011). We also enlarged the spectroscopic dataset of C_3H_8 by incorporating the pseudo line-lists of the ν_7 band (1100–1200 cm^{-1}) and the ν_{21} band (900–940 cm^{-1}) from Sung et al. (2013).

3.1. Thermal profile retrievals

Temperature and haze optical depth vertical profiles were simultaneously retrieved. We derived the haze optical depth from the fit of the observed continuum in the 1080–1120 cm^{-1} spectral range, since this spectral range is free of molecular band emission. The temperature profile was derived from the fit of the ν_4 CH_4 band in the 1200–1330 cm^{-1} spectral range (Fig. 1). The *a priori* temperature profile was the one derived at the equator (from the Tb flyby observations) by Vinatier et al. (2007).

We first determined the vertical shift to apply on the nominal altitude of the line-of-sight extracted from the CIRS database. This nominal altitude usually does not allow us to reproduce perfectly the relative intensity of the Q- and R- or P-branches of the ν_4 CH_4 band. The difference between the nominal and the physical altitude is due to: (i) CIRS navigation pointing errors and (ii) our calculated pressure/altitude grid derived from hydrostatic equilibrium incorporating the *in situ* temperature profile measured by HASI (Fulchignoni et al., 2005) below 120 km, while CIRS observations probe at higher altitudes. So, we ran retrievals of our deepest averaged spectra with different vertical shifts applied to the altitudes of their line-of-sights to infer the one that minimizes the root mean square (rms) residuals between calculated and observed limb spectra (see Appendix B).

After having set the altitude shift, we determined the spectral shift to apply to the observed spectra to obtain the best fit of the 1198–1330 cm^{-1} spectral range, covering the P-, Q- and part of R-branch of the ν_4 CH_4 band. During the Cassini mission, the CIRS reference wavelength laser changed mode about 15 times and the CIRS wavelength nominal calibration was performed by measuring the position of emission lines of methane near 1330 cm^{-1} for each mode. The spectral shift was then estimated to be less than 0.01 cm^{-1} at 1300 cm^{-1} (Brasunas, 2012; Jennings et al., 2017). We ran retrievals with different spectral shifts and kept the one that minimized the rms residuals between calculated and observed limb spectra. We noticed from our extracted datasets that a slight spectral shift of 0.02 cm^{-1} remained, which could be due to the thermal drift of the reference wavelength laser
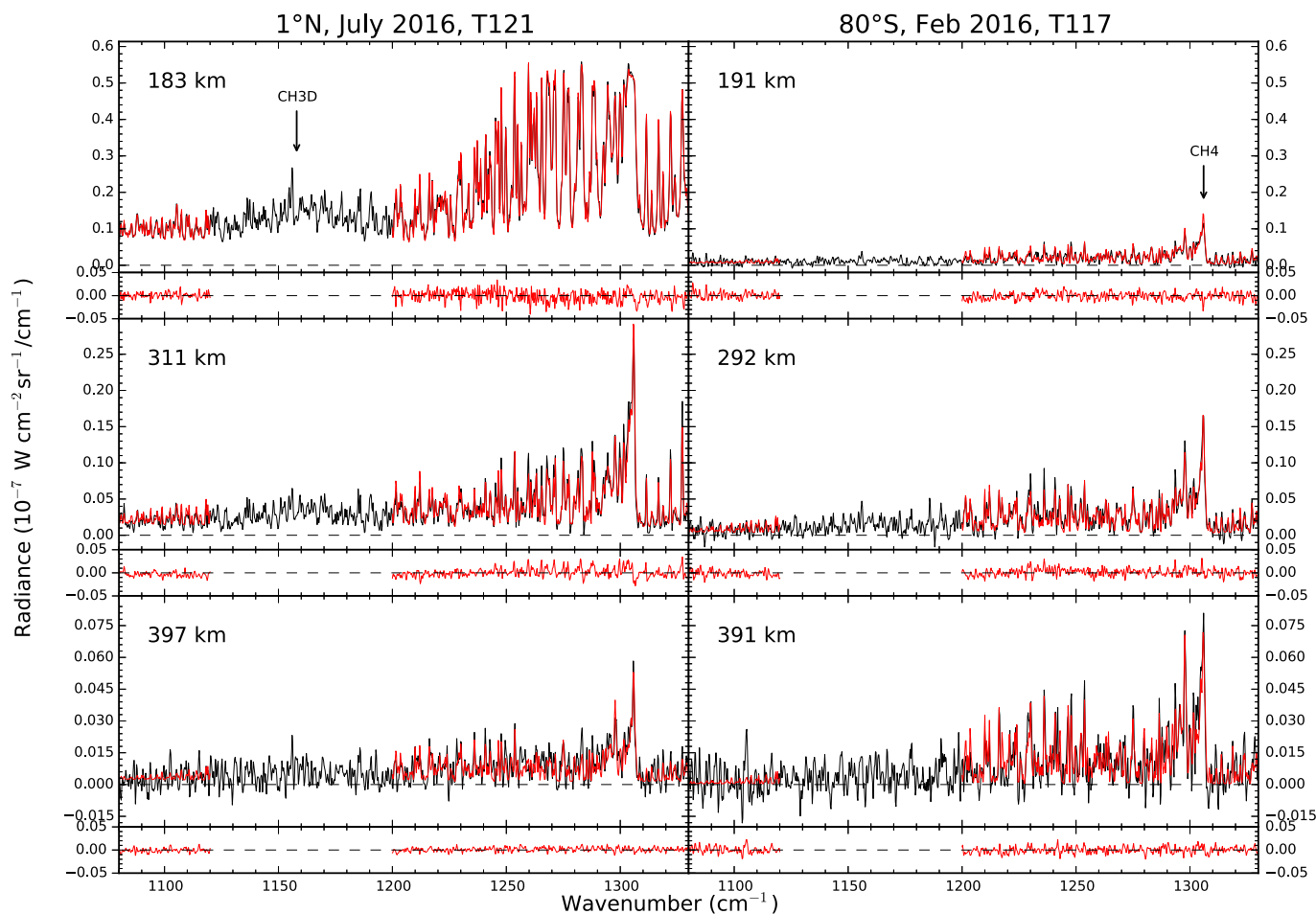

Fig. 1. FP4 limb spectra near the equator (left column) and south pole (right column), during northern spring at similar altitudes. Black lines correspond to the observed spectra and red lines correspond to the synthetic ones calculated in the region used in the inversion process. Residual radiances (observed - synthetic) are also plotted below. The altitudes correspond to the distance of the line-of-sight to the surface corrected by the vertical altitude shift. Molecules are indicated at the center of their bands. (For interpretation of the references to color in this figure legend, the reader is referred to the web version of this article.)

diode. We therefore systematically determined the spectral shift from FP3 and FP4 limb observations independently, since the spectral shift varies with wavenumber.

The 1-σ error on temperature were derived from the contribution of both the propagation of the spectral noise in the retrievals (ΔT_{noise}) and the error ($\Delta T_{\Delta km}$) due to the uncertainty on the applied vertical shift (Δz, see below). The spectral noise contribution to the error bars (ΔT_{noise}) was calculated from the covariance matrix of the solution using a tabulated noise equivalent spectral radiance (NESR), based on early observations during the mission, divided by the square root of the number of spectra as the measurement error. However, the actual NESR varies with the observing sequence and is usually lower than the rms residuals between calculated and observed limb spectra. So we scaled the temperature error ΔT_{noise} due to propagation of the noise by a factor of max(rms)/max(NESR), where max(rms) is the maximum value among all limb spectra of the rms residuals over the 1198–1330 cm^{-1} interval and max(NESR) is the NESR value at 1330 cm^{-1}. Uncertainty on the vertical shift was determined from the rms of the residuals between observed and calculated spectra using different altitude shift values. The 1-σ variation of the rms of the residual around the smallest value (corresponding to our best fit) typically corresponds to a $\Delta z = \pm 2$ km variation. This uncertainty is the same as that determined by Vinatier et al. (2010b) and we verified that it was also valid for our dataset.

$$\Delta T = \sqrt{(\Delta T_{noise})^2 \times \left(\frac{\max(rms)}{\max(NESR)}\right)^2 + (\Delta T_{\Delta km})^2} \qquad (1)$$

For observations in December 2006 (17°N, T21) and January 2007

(4°N, T23), highest limb spectra presented negative continua that we corrected through a procedure described in Appendix C. We added the error contribution of this correction that we estimated as the temperature difference between the retrievals for spectra with negative continuum and those for the corrected spectra. We found a maximum temperature difference of 5 K at high altitude (usually for tangent heights higher than 400 km) where corrupted limb spectra are most easily observed.

We also assessed the information content of our retrieved temperature profiles by using the output profile, modified by typically 5–10 K, as a new input to the retrieval process. We then defined the region of validity of our retrievals as the altitude range where they do not significantly vary with the assumed *a priori* profile.

3.2. Molecular gas volume mixing ratio profile retrievals

The molecules observed in the CIRS FP3 spectral range are: C_2H_2, C_2H_4, C_2H_6, C_3H_8, C_3H_4, C_4H_2, C_6H_6, HCN, HC_3N and CO_2 (Fig. 2). The spectral shift was determined from the fit of the 700–720 cm^{-1} spectral range, which covers the P- and Q-branches of the ν_5 C_2H_2 band and the Q-branch of the ν_2 HCN band. The vertical shifts inferred from the FP4 limb spectra were applied to the FP3 limb spectra. We tested the robustness of the retrieved gas mixing ratio profiles by using different *a priori* profiles. We first used constant-with-height profiles with volume mixing ratio spanning two to three orders of magnitude. Then, we ran a last test using an *a priori* mixing ratio profile corresponding to the convergence zone of the previous retrieved profiles, and above the convergence zone we fixed the profile to a constant value. We finally
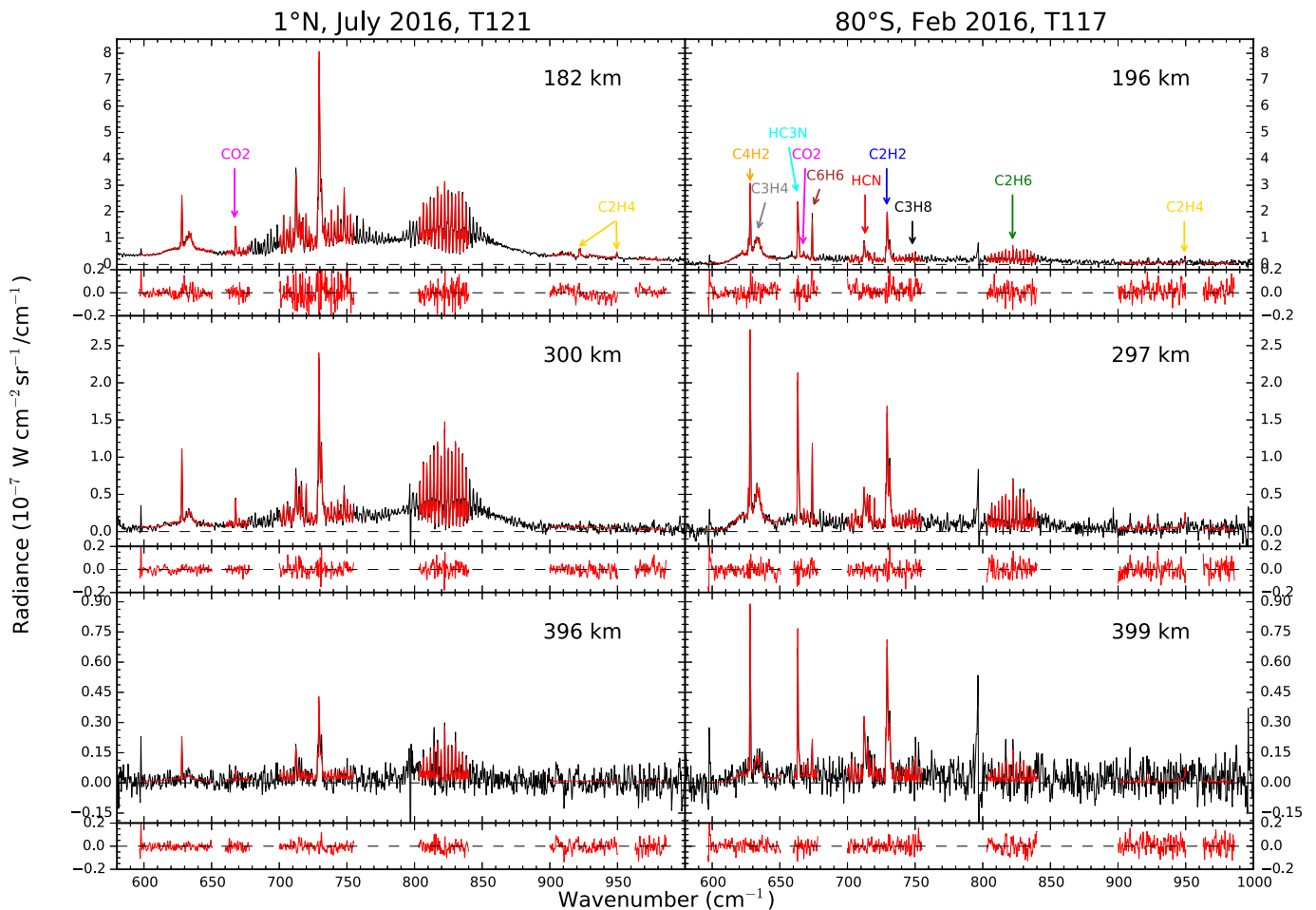

Fig. 2. Same as Fig. 1 for FP3 limb spectra near the equator (left column) and south pole (right column) during northern spring at similar altitudes. The features close to 598 and 795 cm^{-1} are due to instrumental noise.

retained as the region of validity the altitude range where the retrievals do not significantly depend on the *a priori* profile. The haze extinction vertical profile retrieved from the FP4 spectra was used as the *a priori* profile in the retrieval of the haze extinction profile from the FP3 spectral range, taking into account the spectral dependency of the haze opacity derived from Vinatier et al. (2012).

Molecular gas mixing ratio and haze extinction profiles were retrieved simultaneously in a given spectral range. We retrieved in a first step the mixing ratio profiles of C_2H_2 (ν_5 band at 729 cm^{-1}), HCN (ν_2 band at 712 cm^{-1}) and the haze extinction in the 700–740 cm^{-1} spectral range, since C_2H_2 has the most intense emission band in the FP3 spectral range. Then, we retrieved C_2H_6 (ν_9 band at 822 cm^{-1}), C_3H_8 (ν_{26} band at 748 cm^{-1}) mixing ratios and haze extinction from the inversion of limb spectra in the 740–755 and 803–840 cm^{-1} spectral ranges. Next, we retrieved C_3H_4 (ν_9 band at 633 cm^{-1}), C_4H_2 (ν_8 band at 628 cm^{-1}) mixing ratios and haze extinction from the 610–645 cm^{-1} spectral range. HC_3N (ν_5 band at 663 cm^{-1}), CO_2 (ν_2 band at 667 cm^{-1}), C_6H_6 (ν_4 band at 673 cm^{-1}) mixing ratios and haze extinction were retrieved simultaneously from the 660–678 cm^{-1} spectral range. In a last step, we retrieved the C_2H_4 (ν_7 band at 949 cm^{-1}) mixing ratio and haze extinction profiles from the 900–950 and 963–986 cm^{-1} spectral ranges.

For spectra in which C_6H_6 or HC_3N were not detected, we estimated the 2-σ upper limit on their mixing ratios following the methodology described in Nixon et al. (2010).

The total relative error on the retrieved mixing ratio is the quadratic sum of the errors due to the spectral noise propagation $\left(\frac{\Delta q}{q}\right)_{noise}$, the uncertainty on the altitude shift $\left(\frac{\Delta q}{q}\right)_{\Delta km}$ and on the temperature profile $\left(\frac{\Delta q}{q}\right)_{\Delta T}$ (Vinatier et al., 2010b):

$$\frac{\Delta q}{q} = \sqrt{\left(\frac{\Delta q}{q}\right)^2_{noise} \times \left(\frac{\max(rms)}{\max(NESR)}\right)^2 + \left(\frac{\Delta q}{q}\right)^2_{\Delta km} + \left(\frac{\Delta q}{q}\right)^2_{\Delta T}} \qquad (2)$$
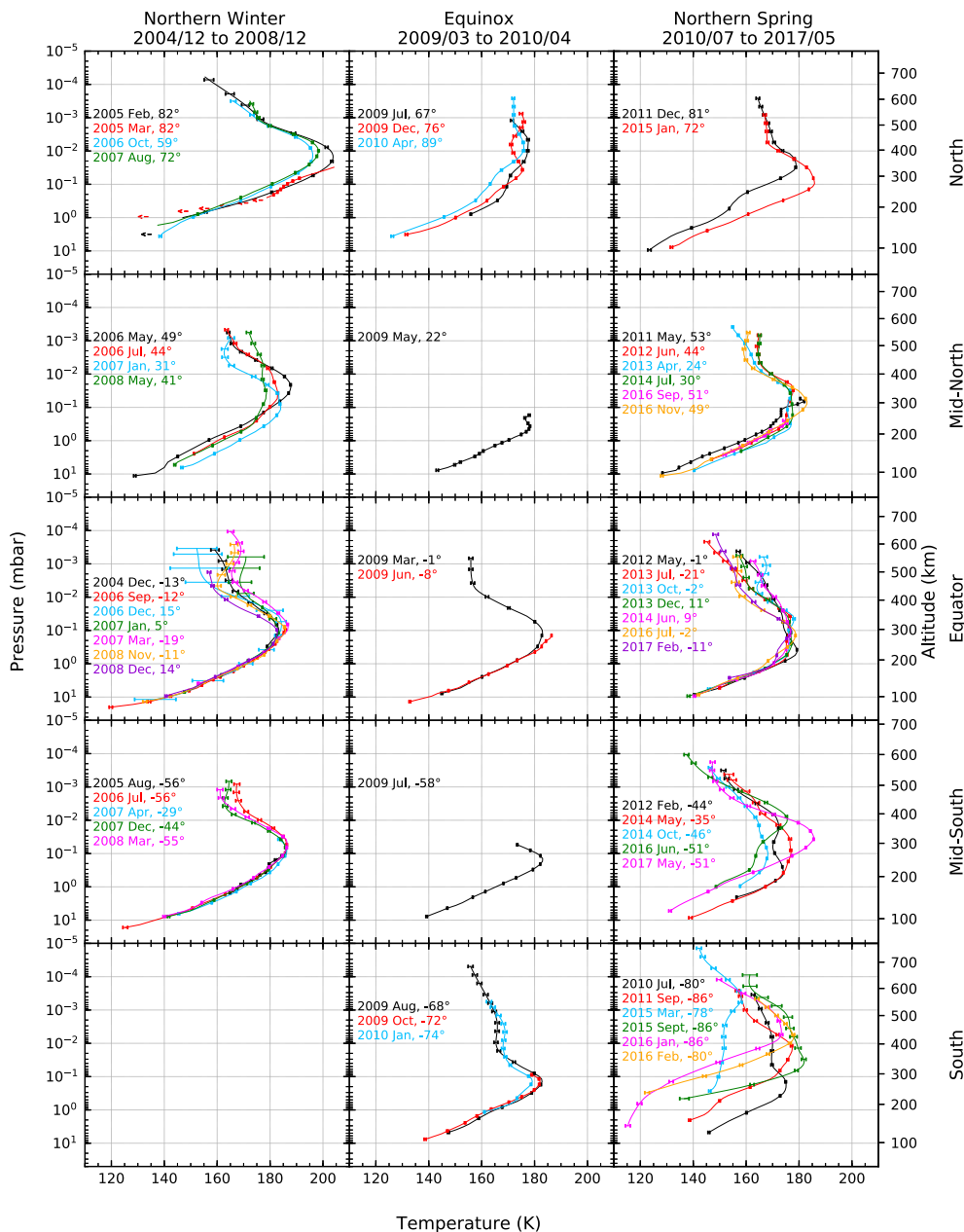

Fig. 3. Thermal profiles in the middle atmosphere of Titan. Each row corresponds to a given latitude region: from top to bottom, north pole to south pole. Each column corresponds to a season: left to right, northern winter to northern spring. On each thermal profile, the 1-σ errors at the pressure level corresponding to the lines-of-sight of the spectra used for the retrievals are plotted. Arrows correspond to 2-σ upper limits. The altitude grid is calculated using the temperature profile of: October 2006 for north, June 2012 for mid-north, May 2012 for equator, June 2016 for mid-south and October 2009 for south.

The uncertainty linked to the altitude shift $\left(\frac{\Delta q}{q}\right)_{\Delta km}$ is the relative difference between the best-fit abundance profile and the abundance profile retrieved with the altitude shift ($\Delta z = \pm 2$ km) applied on the line-of-sight of limb spectra and using the temperature profile inferred with the same altitude shift. The relative uncertainty $\left(\frac{\Delta q}{q}\right)_{\Delta T}$ is the relative difference between the best fit abundance profile and the one retrieved with the minimum or maximum thermal profile determined with ΔT derived from Eq. (1). We determined these relative uncertainties for three cases: T35 (north), T47 (equator), T115 (south) and we considered that they do not vary over the entire studied time period.

4. Results

4.1. Thermal profiles

Fig. 3 shows the thermal profiles retrieved from the limb observations listed in Table 1. These thermal profiles are gathered by latitude range, from top to bottom: north pole (90°N to 60°N), mid-north (60°N to 20°N), equator (20°N to 20°S), mid-south (20°S to 60°S) and south pole (60°S to 90°S) and by season, from left to right: northern winter (December 2004 to December 2008), northern spring equinox (March 2009 to April 2010) and northern spring (July 2010 to May 2017).

4.1.1. High northern latitudes

During northern winter, the northern polar region above 0.1 mbar (~270 km) is hotter than the equatorial region, with a temperature maximum of ~205 K at ~10^{-2} mbar (~400 km) in February 2005 at 82°N, which is the warmest temperature ever observed. In contrast, the northern polar region is colder than the equatorial region below 0.1 mbar (~270 km), e.g. at most 150 K at 1 mbar (~175 km) in 2005 at 82°N *vs* ~170 K in the equatorial region. Near 4 mbar, the temperature in all four profiles is less than 140 K, more than 15 K lower than at equatorial latitudes.

From August 2007 to June 2009, i.e. near northern spring equinox, the northern polar region has been cooling in the $0.3 - 3 \times 10^{-3}$ mbar (~310–430 km) region, by e.g. ~23 K at 10^{-2} mbar (~360 km). In December 2009 at 76°N, the thermal profile presented an oscillation between 4×10^{-2} mbar (~310 km) and 10^{-3} mbar (~490 km) that is discussed in Section 5.3.

During northern spring, from December 2011 to January 2015, the northern polar region warmed up by ~7 K between 10 mbar (~90 km) and 1 mbar (~170 km), and by ~15 K between 1 mbar and 0.1 mbar (~280 km). On the other hand, above 0.02 mbar (~370 km), temperature did not significantly vary in this time lapse. In January 2015, the temperature maximum in the northern polar region was located around 0.1 mbar, two pressure scale heights lower than in 2005, and then similar to the location of the stratopause in the equatorial region.

4.1.2. Northern mid-latitudes

During northern winter, between May 2006 and May 2008, thermal profiles at latitudes poleward of 40°N were ~5 K colder than that at 31°N between 7 mbar (~105 km) and 0.1 mbar (~280 km). The 31°N profile was similar to those in the equatorial region. In contrast, thermal profiles above 40°N were ~10 K warmer above 0.02 mbar (~370 km) than the one at 31°N. At these latitudes, the temperature around 0.02 mbar decreased from ~190 K in May 2006 to ~177 K in May 2008.

Around northern spring equinox in May 2009, the temperature profile at 22°N was close to the profile at 31°N in January 2007 between 9 mbar (~100 km) and 0.5 mbar (~210 km), but colder in the 0.2 –0.5 mbar region. These data are at high vertical resolution (~10 km) and do not extend higher than 0.1 mbar (~285 km).

During northern spring, the stratosphere warmed up by about 3 K between 5 mbar (~120 km) and 0.3 mbar (~235 km) from May 2011

(53°N) to June 2012 (44°N). The temperature profile was roughly isothermal between 0.3 mbar and 0.04 mbar (~330 km) from June 2012 to July 2014 (*T* ~175 K). In November 2016, the temperature had increased in this altitude region, reaching a maximum of 183 K at 0.08 mbar (~295 km).

4.1.3. Equatorial latitudes

Over the Cassini mission, the lower stratosphere, below the 0.5-mbar level, did not show temperature variations in excess of 5 K at equatorial latitudes. In the 0.1-mbar region, we do not observe strong variations between December 2004 and June 2009 (T~175 K), while in the 2012–2017 period, the temperature is ~7 K lower. Higher, around 0.01 mbar, the situation is less clear but the temperature overall decreases by some 10 K between 2012 and 2017. In the μbar region, thermal profiles show variations over the mission that are correlated neither with latitude nor local time.

4.1.4. Southern mid-latitudes

During southern summer (2004–2008), temperature profiles at southern mid-latitudes did not present strong variations and were quite similar to those around the equator at the same period.

Near southern autumn equinox, in July 2009 at 58°S, the stratosphere had slightly cooled, by ~2 K between 8 mbar (~110 km) and 0.07 mbar (~310 km), compared with southern summer conditions.

During southern autumn, the atmosphere in February 2012 (44°S) was ~2 K warmer between 10 mbar (~100 km) and 1 mbar (~185 km) than that in July 2009 (58°S), while above the 1-mbar level the temperature was lower. The temperature minimum observed in the 44°S-profile near 0.05 mbar (~320 km) could be due to an oscillation as it is not present in the thermal profile in May 2014 (35°S). This oscillation is similar to that observed in December 2009 at 74°N and discussed in Section 5.3. Between May 2014 (35°S) and October 2014 (46°S), the temperature decreased between 1 mbar (~180 km) and 2×10^{-4} mbar (~575 km), e.g. by ~8 K at 0.1 mbar (~275 km). Then in June 2016 (51°S), the atmosphere above 0.05 mbar (~300 km) had warmed up compared to October 2014 (46°S), by ~11 K at 0.01 mbar (~375 km), the local temperature maximum, and cooled down below 0.05 mbar by ~6-7 K. Between June 2016 and May 2017 (51°S), the temperature strongly increased between 0.3 mbar (~225 km) and 0.01 mbar (~390 km), by up to ~20 K at 0.04 mbar (~320 km), which is the local temperature maximum. In the lower stratosphere (0.5-5 mbar), the atmosphere cooled by approximately 15 K between 2012 and 2017.

4.1.5. High southern latitudes

During southern summer, CIRS did not record limb spectra at 0.5-cm^{-1} spectral resolution in the south polar region.

Around southern autumn equinox, temperature profiles at high southern latitudes did not present strong variations between August 2009 and January 2010, being actually similar to the thermal profile near the equator in March 2009 below the 0.05-mbar level. Still, we observed a slight cooling between 0.7 mbar (~195 km) and 0.03 mbar (~350 km) during this period, reaching ~5 K at 0.1 mbar (~290 km), while between 0.03 mbar and 0.001 mbar (~520 km) the temperature increased by ~3 K.

The evolution of the temperature profiles is much more dramatic during southern autumn between 2010 and 2016. At first, we observe a limited decrease in temperature between January 2010 (74°S) and July 2010 (80°S) in the range 0.4–0.05 mbar (~220-320 km), reaching ~3 K at 0.2 mbar (~255 km), and a slight increase in the range 0.01 –0.001 mbar (~395-510 km). Fourteen months later, in September 2011 (86°S), temperature had increased in the range 0.08 -4 × 10^{-3} mbar (~280-430 km), by as much as ~7 K at 0.01 mbar (~380 km), while the region below the 0.08-mbar level strongly cooled, e.g. by ~16 K at 1 mbar (~175 km). In March 2015 (78°S), the whole region below the 4×10^{-4}-mbar (~500 km) region had strongly cooled compared to September 2011, by as much as ~26 K at 0.01 mbar (~350 km). Only six

months later, in September 2015 (86°S), we observe a strong increase in temperature below the 10^{-4}-mbar region (~595 km), reaching ~31 K at 0.04 mbar (~285 km). A few months later, in January (86°S) and February (80°S) 2016, the thermal profiles had strongly cooled down below 0.01 mbar (~325 km), by as much as ~30 K at 0.2 mbar (~210 km), while they had not changed much above this pressure level.

4.2. Molecular gas volume mixing ratio profiles

Figs. 4–13 show the gas mixing ratio profiles of: C_2H_2, C_2H_4, C_2H_6, C_3H_4, C_3H_8, C_4H_2, C_6H_6, HCN, HC_3N and CO_2 retrieved using the limb observations listed in Table 1.

Carbon dioxide (CO_2) does not exhibit strong seasonal variations at any latitude. The profiles show a local maximum around 1 mbar (~190 km) at all latitudes, except during the northern winter at high northern latitudes (Fig. 4). The peak-to-peak amplitude of this variation is at most a factor of two. We will not discuss further the CO_2 mixing

ratio profiles in the following sections.

4.2.1. High northern latitudes

Seasonal changes of abundance profiles in the northern polar region are also shown in Fig. 14. During northern winter, from February 2005 to August 2007, the abundances of most photochemical compounds between 10 mbar (~100 km) and 10^{-4} mbar (~690 km) were larger than at equatorial latitudes at the same season. The difference amounts to a factor of 3-5 for C_3H_4, C_4H_2, C_2H_4, C_6H_6 and a factor of 50 for HC_3N at 1 mbar (~175 km). On the other hand, the C_2H_6 and C_3H_8 profiles did not show significant differences with their equatorial counterparts. During this period, we also detected benzene below 0.01 mbar (~400 km) with a mole fraction of ~4×10^{-9} at 80°N, 10^{-9} at 70°N, and $3–5 \times 10^{-10}$ at 50°N.

In December 2009 and April 2010, shortly after northern spring equinox, we observed an enrichment in photochemical compounds above 0.1 mbar (~260 km), compared to July 2009. In particular,
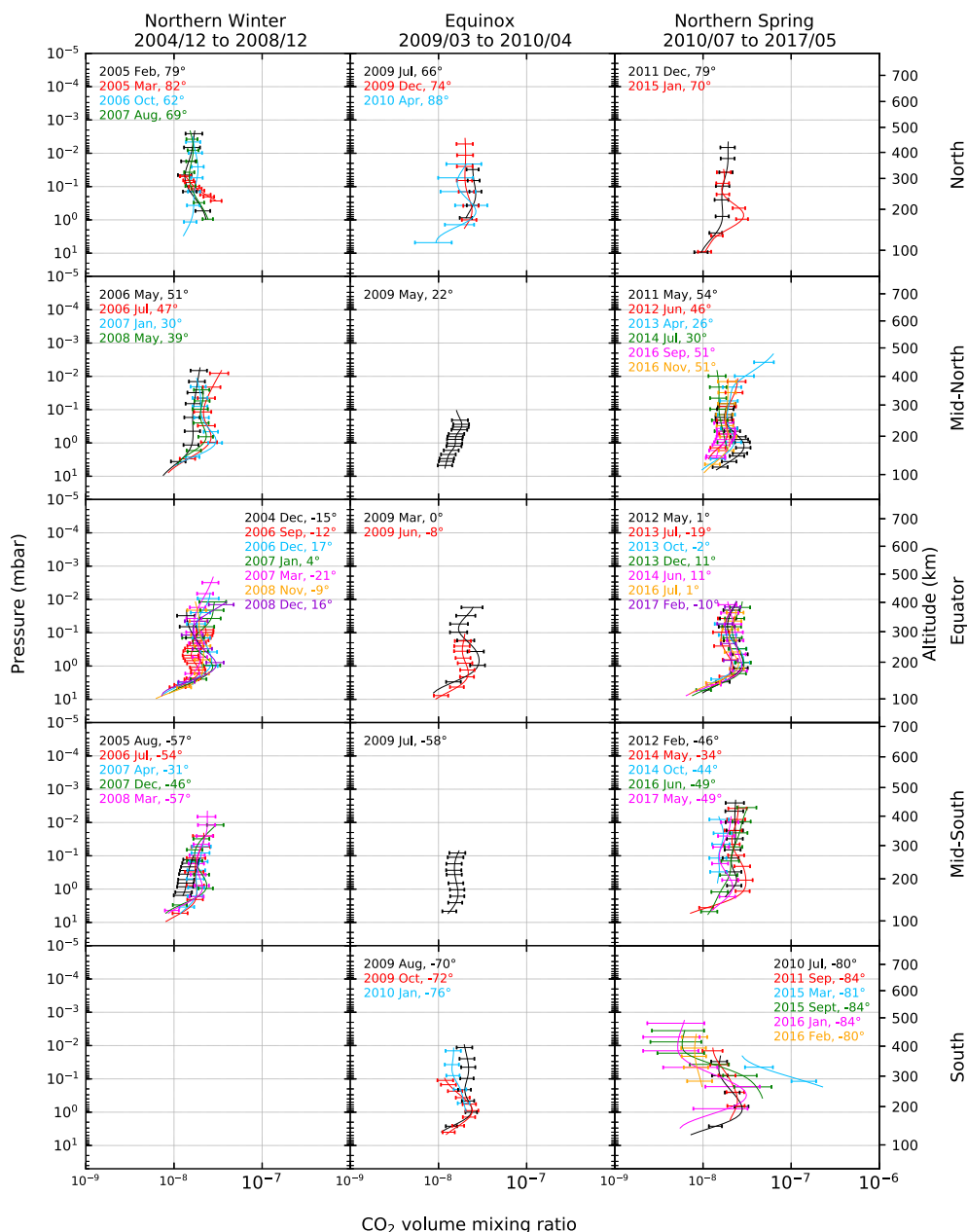

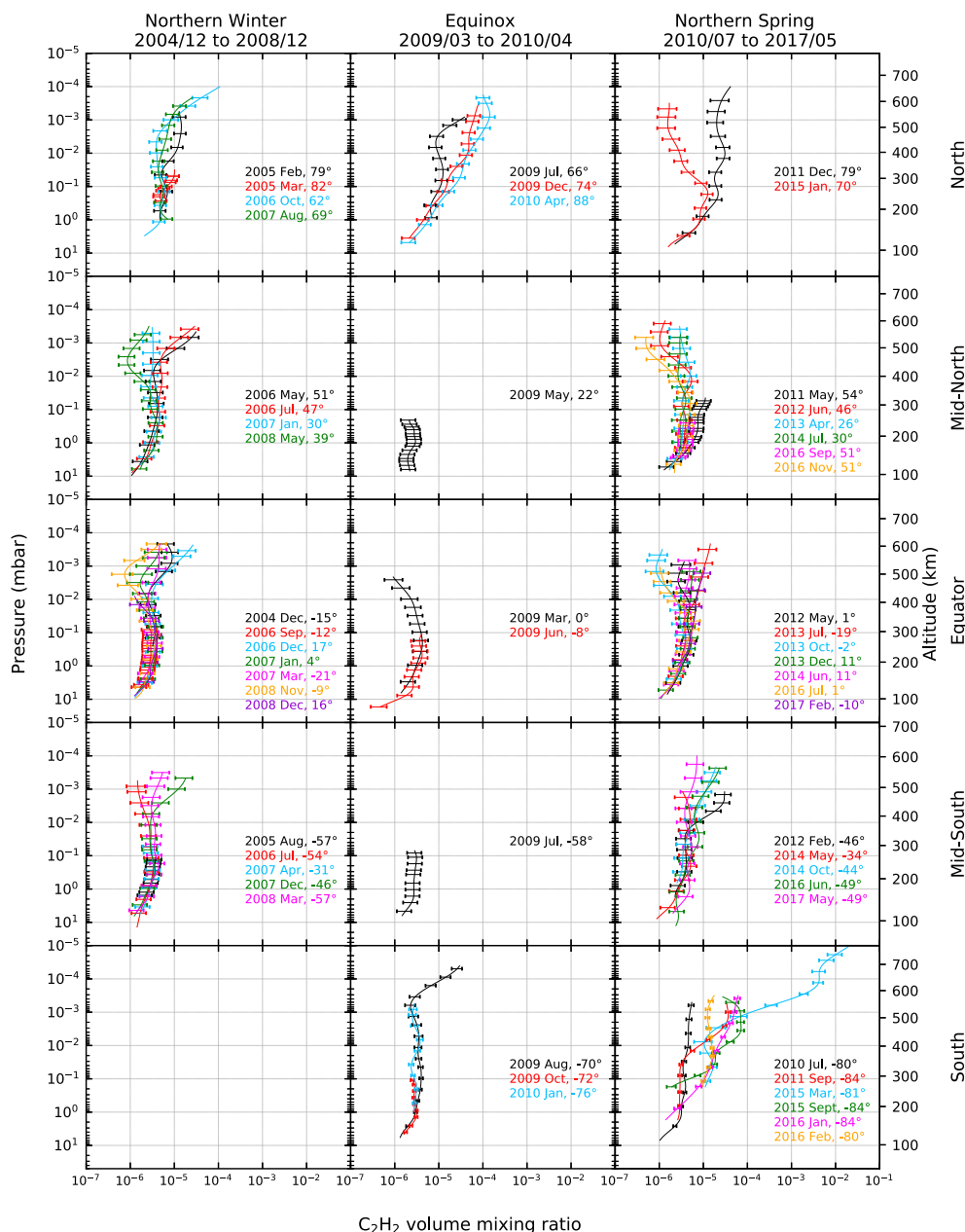**Fig. 4.** CO_2 gas volume mixing ratio profiles in the middle atmosphere of Titan. Same format as Fig. 3.

Fig. 5. C_2H_2 gas volume mixing ratio profiles in the middle atmosphere of Titan. Same format as Fig. 3.

benzene was detected up to the 10^{-4}-mbar level (~630 km). We can also note that C_2H_2 was more abundant than C_2H_6 at pressures less than a few 10^{-2} mbar (~375 km) (Fig. 14).

In the beginning of northern spring in December 2011, we observed a global depletion in molecules, except for C_2H_6, above 0.1 mbar (~260 km) with respect to the April 2010 profiles. We also observed that the C_2H_2 abundance profile was similar to the C_2H_6 profile, and that benzene was only observed below the 0.01-mbar (~375 km) level with a mixing ratio of a few 10^{-10} at 79°N. Then in January 2015, the depletion in molecules above 0.1 mbar (~280 km) was even more pronounced than in December 2011, by factors of ~12, ~8 and ~3 for C_2H_2, C_4H_2 and HCN respectively, at 1×10^{-3} mbar (~480 km).

4.2.2. Mid and equatorial latitudes

Between 60°N and 60°S in the stratosphere below 0.01 mbar (~410 km), photochemical compounds are slighly more abundant during northern winter season than in northern spring. Above 0.01 mbar, C_2H_2 and HCN abundance profiles show variations that do not seem

correlated with year or local time (see Table 1).

However, we observe in some specific cases abundance variations at latitudes close to the winter polar vortex. In May 2006 (51°N), a local maximum of the HC_3N mixing ratio occurs at 0.1 mbar (~290 km), as is the case at 62°N in October 2006. Around 45°S, we observed an enrichment in all photochemical compounds below 0.1 mbar (~290 km) between October 2014 and June 2016, as is seen at higher southern latitudes (Section 4.2.3).

4.2.3. High southern latitudes

Seasonal changes of abundance profiles in the southern polar region are also shown in Fig. 15. From August 2009 (70°S) to at least July 2010 (80°S), we did not observe strong variations in any abundance profile between 10 mbar (~95 km) and 10^{-3} mbar (~520 km). In September 2011, during southern autumn, we observed a strong and global enrichment in photochemical products compared to June 2010 between 10^{-2} mbar (~380 km) and 10^{-4} mbar (~620 km). This enrichment reaches a factor of 100–1000 for molecules such as C_3H_4, C_4H_2, HC_3N,
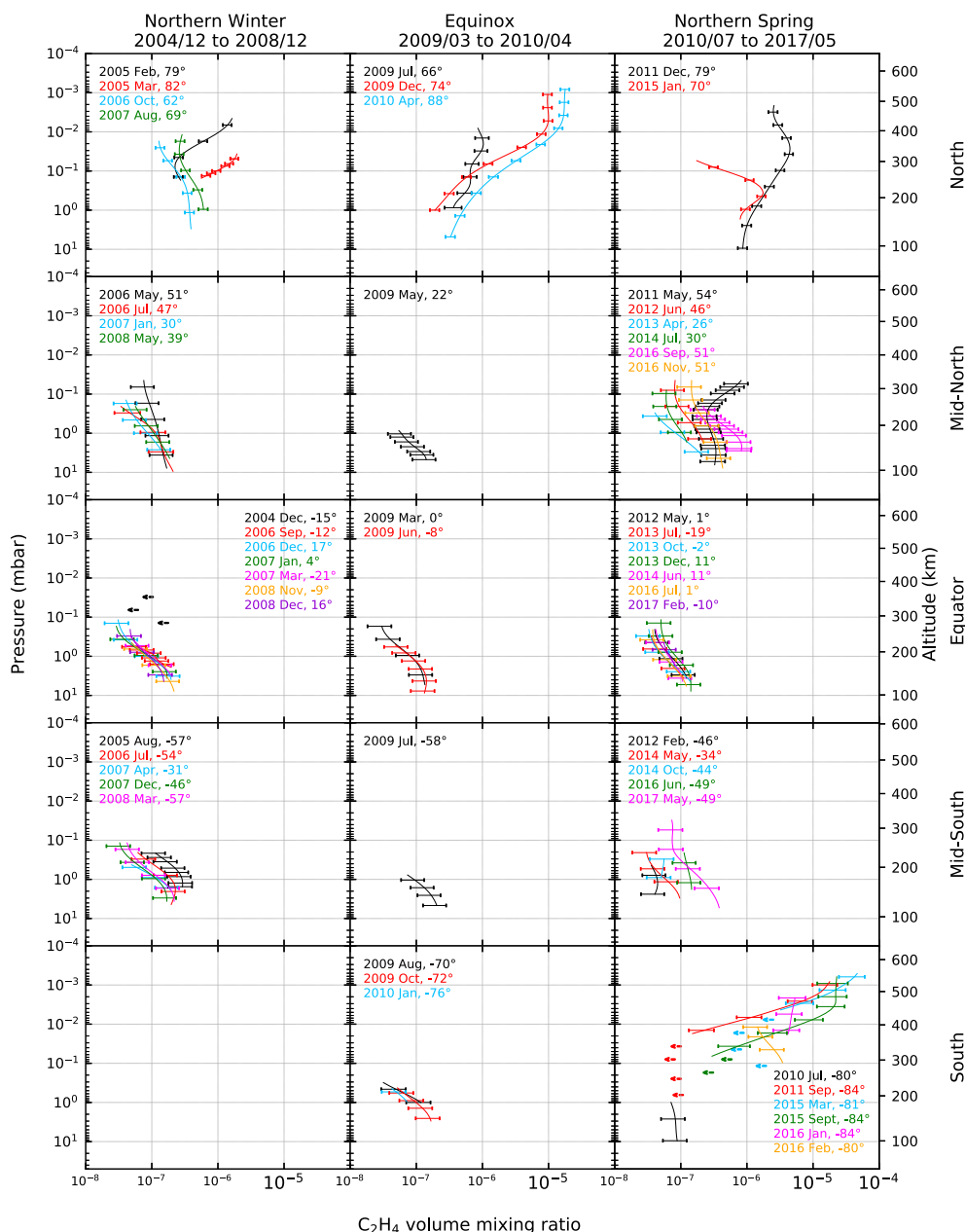
Fig. 6. C_2H_4 gas volume mixing ratio profiles in the middle atmosphere of Titan. Same format as Fig. 3.

C_2H_4 and a factor of 10 for molecules such as C_2H_2, HCN. At this date, we also detected benzene in the southern polar region above 2×10^{-3} mbar (~465 km) with a mixing ratio of at least 10^{-7}–10^{-6}. Then by March 2015, molecular abundances had continued to increase, being larger than in September 2011 by a factor of 10 above 10^{-3} mbar (~455 km). Between 0.1 mbar (~255 km) and 10^{-3} mbar (~455 km), C_2H_2 and HCN mixing ratios were larger by factors of 3 and 10 respectively. In September 2015, only six months later, the abundances of the photochemical compounds had significantly decreased near and above 10^{-3} mbar (~475 km) but were still larger than inferred around southern autumn equinox. This decrease continued at a lower pace in the 10^{-3}-mbar region till January 2016. One month later, the abundance profiles we inferred were relatively constant with height between 0.1 mbar (~230 km) and 10^{-3} mbar (~450 km), except for HCN which showed a factor of 3 variation over this altitude range.

5. Discussion

5.1. Equatorial mixing ratio profiles compared with photochemical models

We have shown that temperature and volume mixing ratio profiles do not change significantly over seasons at the equator from 10 (~90 km) to 0.01 mbar (~290 km), which is consistent with previous CIRS investigations (Achterberg et al., 2008; Sylvestre et al., 2018; Teanby et al., 2019; Vinatier et al., 2015). On the other hand, we found that the C_2H_2 (acetylene) mole fraction varies in the mesosphere above 10^{-2} mbar (~400 km) without any correlation with the local time (see Table 1). Such variations are not currently explained.

If we focus on the 10–0.01 mbar region, our derived C_2H_2 abundance profiles show a local maximum at ~0.2 mbar (~265 km) that it is not predicted by photochemical models (Dobrijevic et al., 2016; Krasnopolsky, 2014; Loison et al., 2015; Vuitton et al., 2019). At 0.2 mbar, the
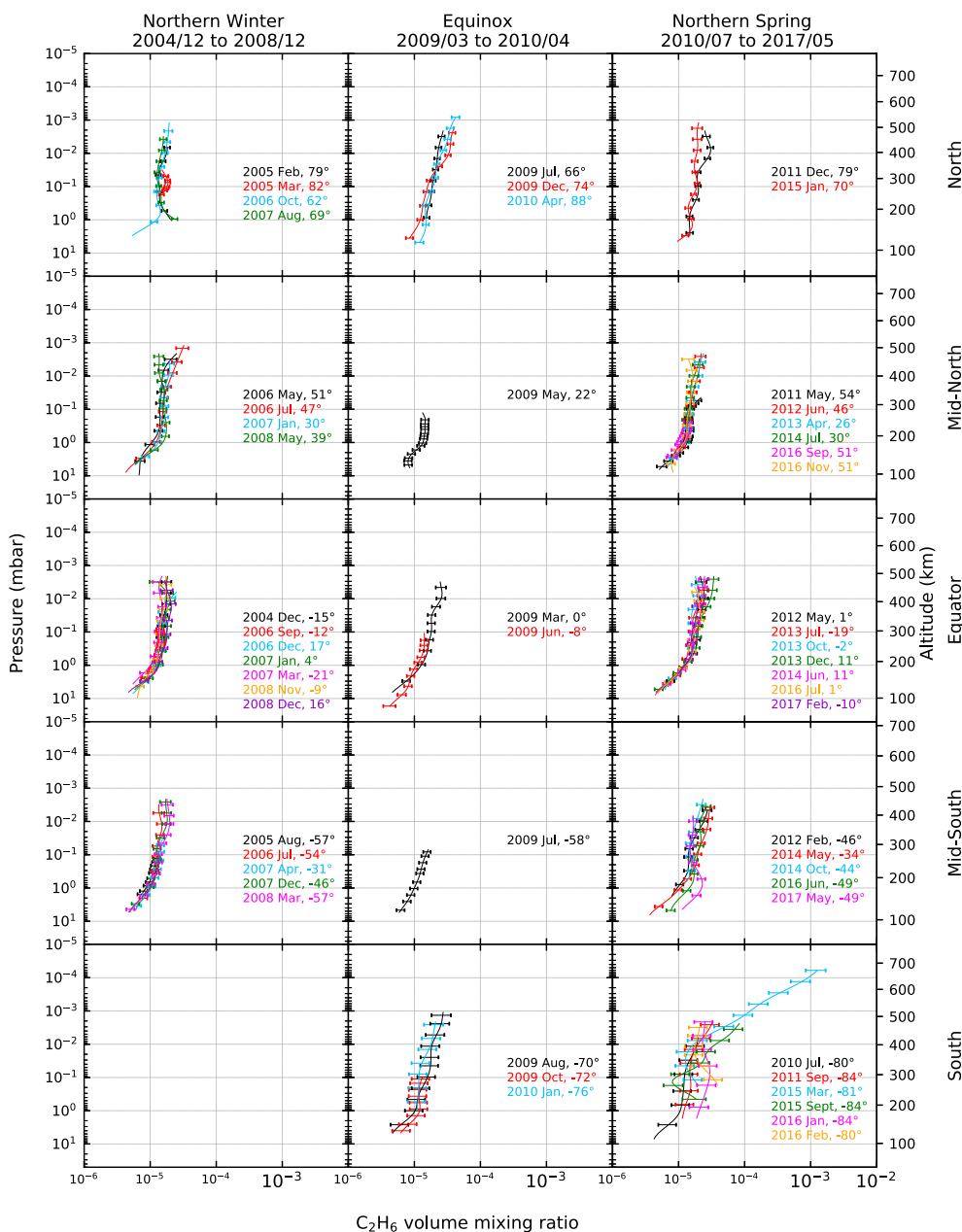
Fig. 7. C_2H_6 gas volume mixing ratio profiles in the middle atmosphere of Titan. Same format as Fig. 3.

observed C_2H_2 volume mixing ratio of $\sim 4 \times 10^{-6}$ is consistent within a factor of 2 with photochemical model predictions. The C_2H_2 abundance derived in November 2008 at 5×10^{-4} mbar (~ 500 km) is consistent with the Cassini/UVIS C_2H_2 abundance derived in February 2008 at 550 km at 6°S (Koskinen et al., 2011). Above 550 km, our retrieved C_2H_2 profiles are quite consistent with C_2H_2 profiles derived from VIMS spectra (Dinelli et al., 2019).

Our inferred HCN (hydrogen cyanide) equatorial abundance profiles show a local maximum around 0.3 mbar (~ 245 km) and a local minimum around 0.01 mbar (~ 410 km), both of which are not reproduced by photochemical models (Dobrijevic et al., 2016; Krasnopolsky, 2014; Loison et al., 2015; Vuitton et al., 2019), while at 0.3 mbar, the derived mixing ratio of $\sim 10^{-6}$ agrees with these model predictions. We note that the eddy mixing coefficient plays an important role in the HCN profile as simulated by Vuitton et al. (2019) who obtained the best match with our retrieved profiles using an eddy mixing coefficient having a minimum value $K_0 \sim 100$ cm^2 s^{-1}, instead of $K_0 = 300$ cm^2 s^{-1}

in the nominal model. In November 2008, our HCN abundance at 500 km ($\sim 7 \times 10^{-6}$) is consistent with the mixing ratio derived from UVIS stellar occultation measurements at 550 km in February 2008 at 6°S (Koskinen et al., 2011). Above 550 km, our retrieved HCN profiles are less abundant than those derived from VIMS spectra (Dinelli et al., 2019).

The C_2H_4 (ethylene) mixing ratios we inferred around 0.1 mbar (~ 290 km) are consistent with predictions of the photochemical models of Krasnopolsky (2014), Loison et al. (2015) and Dobrijevic et al. (2016), but less abundant by a factor of 5 than that of Vuitton et al. (2019). From 5 to 0.1 mbar, the negative vertical gradient we derived is at odds with these photochemical models. According to Crespin et al. (2008), it is explained by the fact that C_2H_4 does not condense in Titan's conditions and by dynamical advection that transports air enriched in C_2H_4 from the winter pole towards the equator in the lower stratosphere.

For C_3H_8 (propane), the inferred abundance profiles at the equator are consistent in the range 10–0.01 mbar (~ 90–410 km) with the
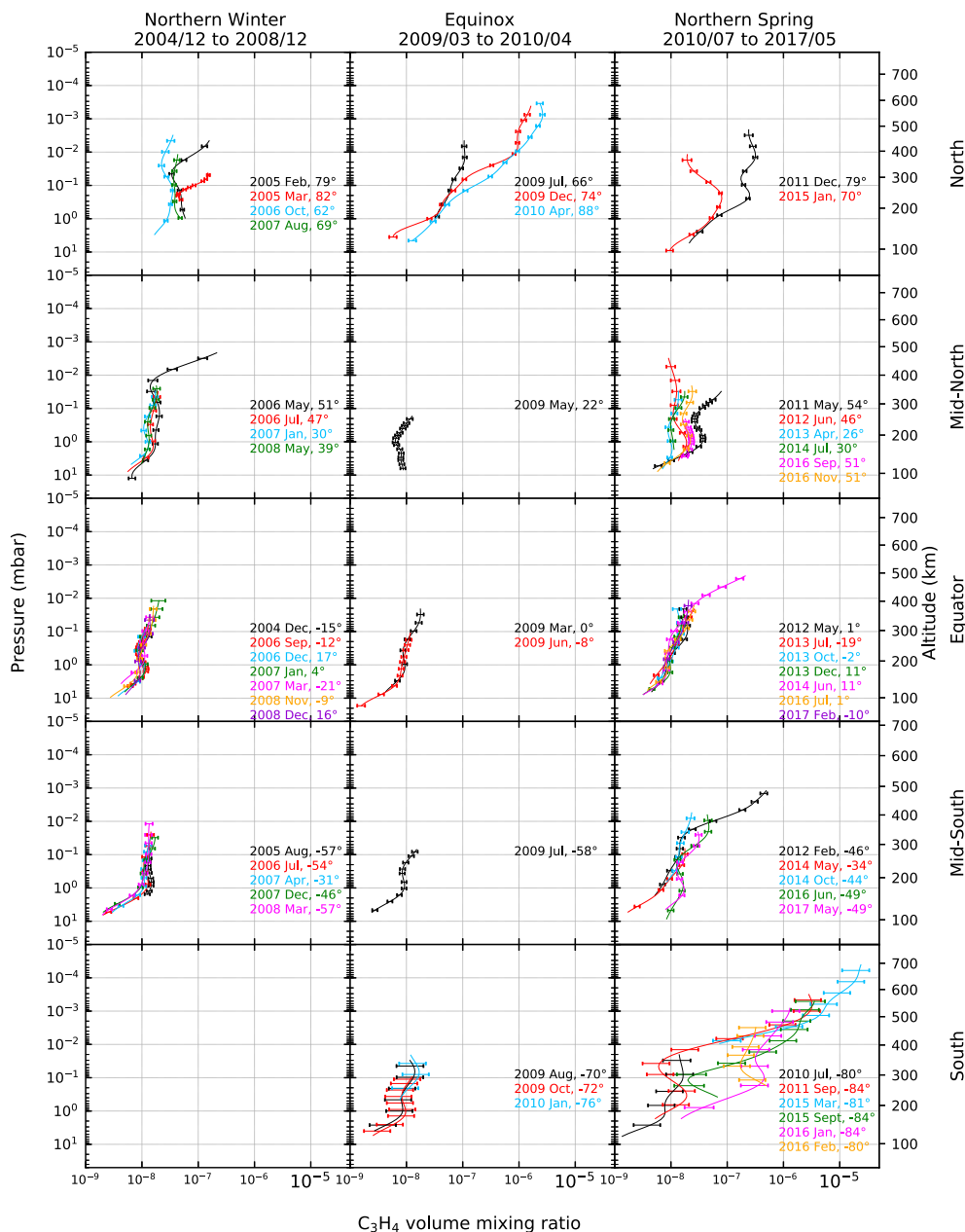
Fig. 8. C$_3$H$_4$ gas volume mixing ratio profiles in the middle atmosphere of Titan. Same format as Fig. 3.

photochemical model predictions of Krasnopolsky (2014), Loison et al. (2015), Dobrijevic et al. (2016) and Vuitton et al. (2019).

Regarding C$_3$H$_4$ (methylacetylene), our abundance profiles show a mixing ratio almost constant with height between 3 mbar ($\sim$140 km) and 0.1 mbar ($\sim$300 km), which is consistent with Vuitton et al.'s (2019) and Krasnopolsky's (2014) photochemical models, while in this altitude range, Loison et al.'s (2015) and Dobrijevic et al.'s (2016) photochemical models predict a C$_3$H$_4$ abundance decreasing with height. At 0.02 mbar, our C$_3$H$_4$ mixing ratios in January 2007 and after 2012 are consistent with these photochemical models. In June 2014 above 0.01 mbar ($\sim$410 km), we derived a positive abundance gradient consistent with Vuitton et al.'s (2019) photochemical model, while this change of slope is observed at 600 km in Loison et al.'s (2015) and Dobrijevic et al.'s (2016) models and at 300 km in Krasnopolsky's (2014) photochemical model.

The C$_4$H$_2$ (diacetylene) abundance profiles retrieved during the northern winter between 0.8 mbar ($\sim$200 km) and 0.01 mbar

($\sim$410 km) are in agreement with the predicted abundance profile of Dobrijevic et al.'s (2016) photochemical model, and with the Vuitton et al. (2019) photochemical model with no H heterogeneous loss reaction. Krasnopolsky's (2014) photochemical model predicts a C$_4$H$_2$ abundance profile with a strong positive gradient in this altitude region that we do not observe. Dobrijevic et al.'s (2016) and Vuitton et al.'s (2019) photochemical models predict a local mixing ratio minimum around 500 km that is not observed in our C$_4$H$_2$ abundance profiles at any season. On the other hand, these photochemical models exhibit a positive abundance gradient above 500 km that we observe above 0.01 mbar ($\sim$410 km) during the northern winter. At higher altitudes, our C$_4$H$_2$ mixing ratio of $\sim$7 $\times$ 10^{-7} at 5 $\times$ 10^{-4} mbar ($\sim$560 km) during the northern winter is consistent with the derived UVIS value of 5 $\times$ 10^{-7} around 500 km in February 2008 at 6°S (Koskinen et al., 2011). During the northern spring, our C$_4$H$_2$ profiles show a positive abundance gradient between 10 mbar ($\sim$90 km) and 10^{-3} mbar ($\sim$530 km) that is not as strong as the gradient in Krasnopolsky's (2014) photochemical
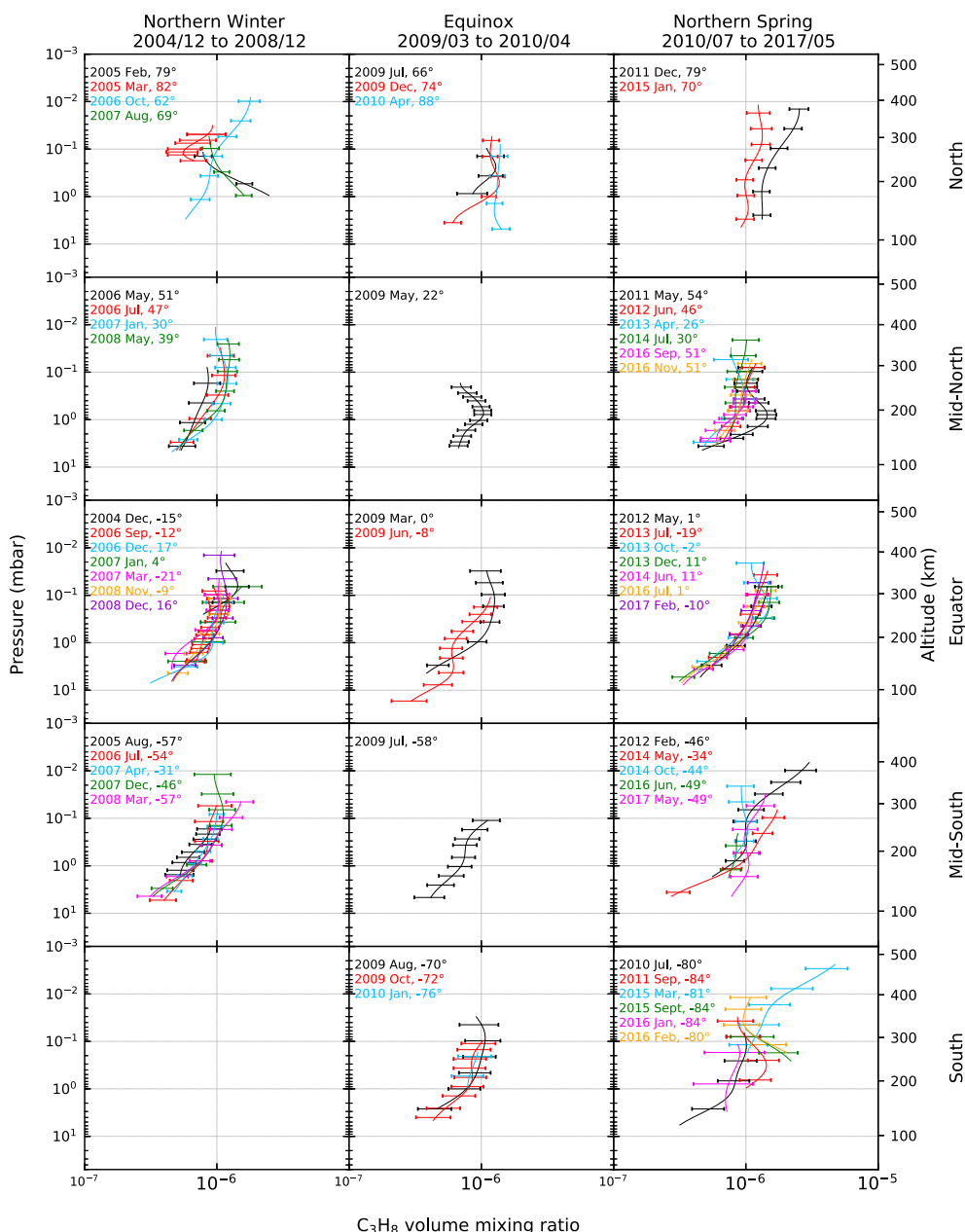
Fig. 9. C_3H_8 gas volume mixing ratio profiles in the middle atmosphere of Titan. Same format as Fig. 3.

model, and is not predicted by Dobrijevic et al. (2016) and Vuitton et al. (2019).

We were able to detect HC_3N (cyanoacetylene) emission at altitudes up to 590 km (2–3× 10^{-4} mbar) during the northern winter, which is higher than what was achieved in a previous study at the equator (Vinatier et al., 2015). The present detection of HC_3N at high altitude results from the improvement of the signal-to-noise ratio in limb spectra due to the upgraded calibration and our averaging procedure described in Appendix B. HC_3N reaches a volume mixing ratio of 2×10^{-6} at ~3×10^{-4} mbar (~580 km), quite consistent with the ~10^{-6} value derived at 550 km in February 2008 at 6°S from UVIS stellar occultations (Koskinen et al., 2011). At 3×10^{-4} mbar, our HC_3N mixing ratio values are ~14 times larger than the predicted value of Vuitton et al. (2019) when they use the aerosol optical depth from Lavvas et al. (2010) multiplied by a factor of 2. Indeed, HC_3N is strongly sensitive to UV photodissociation, so the higher the aerosol opacity the lower the photodissociation efficiency of HC_3N because of aerosol UV-shielding. In

Loison et al.'s (2015) and Dobrijevic et al.'s (2016) models, which incorporate a different aerosol optical depth profile, the HC_3N mixing ratios are ~300 times smaller than our value at 3×10^{-4} mbar. In contrast, our HC_3N mixing ratios are a factor of 30 smaller than in Krasnopolsky's (2014) photochemical model, in which the aerosol optical depth model derives from Huygens observations. During the northern winter, we did not find the local minimum in the mixing ratio predicted at 500 km by photochemical models (Dobrijevic et al., 2016; Krasnopolsky, 2014; Loison et al., 2015; Vuitton et al., 2019).

Regarding CO_2 (carbon dioxide), our abundance profiles are consistent with Krasnopolsky's (2012) photochemical model, but are higher than the Loison et al. (2015) and Vuitton et al. (2019) profiles by an order of magnitude. Interestingly, we observe a local maximum at 1 mbar (~190 km) and a local minimum at 0.1 mbar (~300 km), which are not predicted by photochemical models (Krasnopolsky, 2012; Loison et al., 2015; Vuitton et al., 2019). This local maximum is also observed at mid-latitudes and at the south pole and seems to be stable with season.
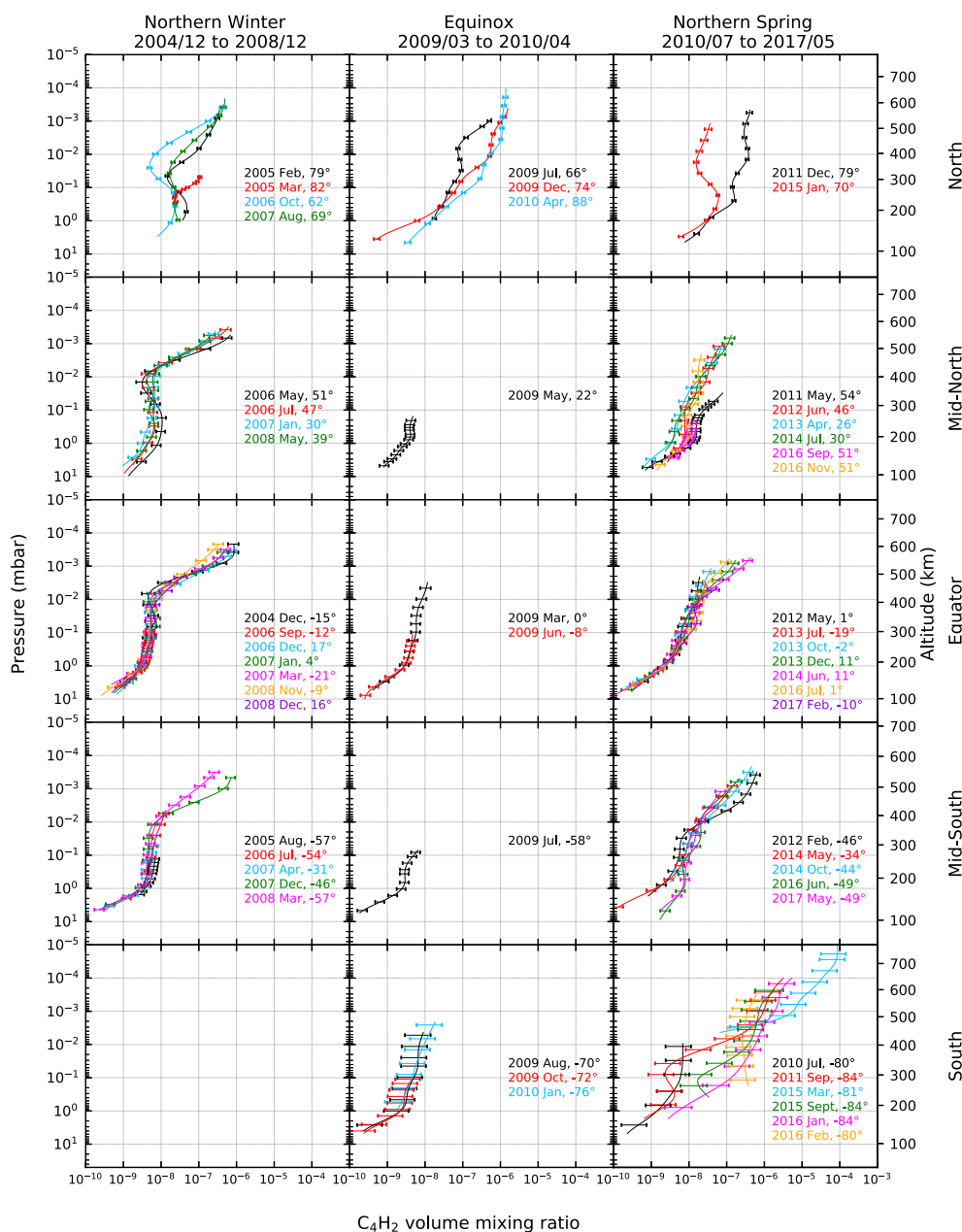
Fig. 10. C$_4$H$_2$ gas volume mixing ratio profiles in the middle atmosphere of Titan. Same format as Fig. 3.

Our inferred C$_2$H$_6$ (ethane) abundance profiles are quite consistent with the Vuitton et al. (2019) photochemical model when they use a minimum value of the eddy mixing coefficient somewhat lower than the nominal value of 300 cm^2 s^{-1} or when they use half of the aerosol optical depth from Lavvas et al. (2010). As for HC$_3$N, UV aerosol shielding limits the efficiency of the photodissociation. In Vuitton et al.'s (2019) model, the C$_2$H$_6$ abundance is very sensitive to the aerosol optical depth, since for a nominal aerosol optical depth C$_2$H$_2$ is less photodissociated, which leads to less C$_2$H and CH$_3$ radicals, the precursors of C$_2$H$_6$. The C$_2$H$_6$ profiles predicted by the photochemical models of Loison et al. (2015) and Dobrijevic et al. (2016), who used different aerosol depth profile and CH$_3$ recombination rate, are consistent with our retrieved profile. Krasnopolsky's (2014) photochemical model, with an aerosol optical depth model based on Huygens observations and a different CH$_3$ recombination rate, has half less ethane than observed between 100 and 250 km, and above this altitude range, the predicted strong abundance gradient is not consistent with our C$_2$H$_6$ abundance profiles.

Regarding C$_6$H$_6$ (benzene), we could only obtain 2-σ upper limits of its mixing ratio between 20 mbar ($\sim$80 km) and 0.01 mbar ($\sim$410 km), except for December 2006 where we could detect its emission band. According to photochemical models, the low abundance of C$_6$H$_6$ below the production region results from efficient photodissociation to phenyl radicals throughout the bulk of the atmosphere. At 10 mbar ($\sim$100 km), our upper limits do not exceed a few 10^{-10}, consistent with Vuitton et al.'s (2019) and Krasnopolsky's (2014) photochemical models that predict a mixing ratio not exceeding 10^{-10} or a few 10^{-9} at this altitude, respectively.

5.2. Evolution of polar regions

5.2.1. Northern polar region

In February 2005, the temperature profile in the northern polar region is warmer between 0.3 mbar ($\sim$230 km) and 3 $\times$ 10^{-3} mbar ($\sim$480 km) than the temperature profile around the equator in
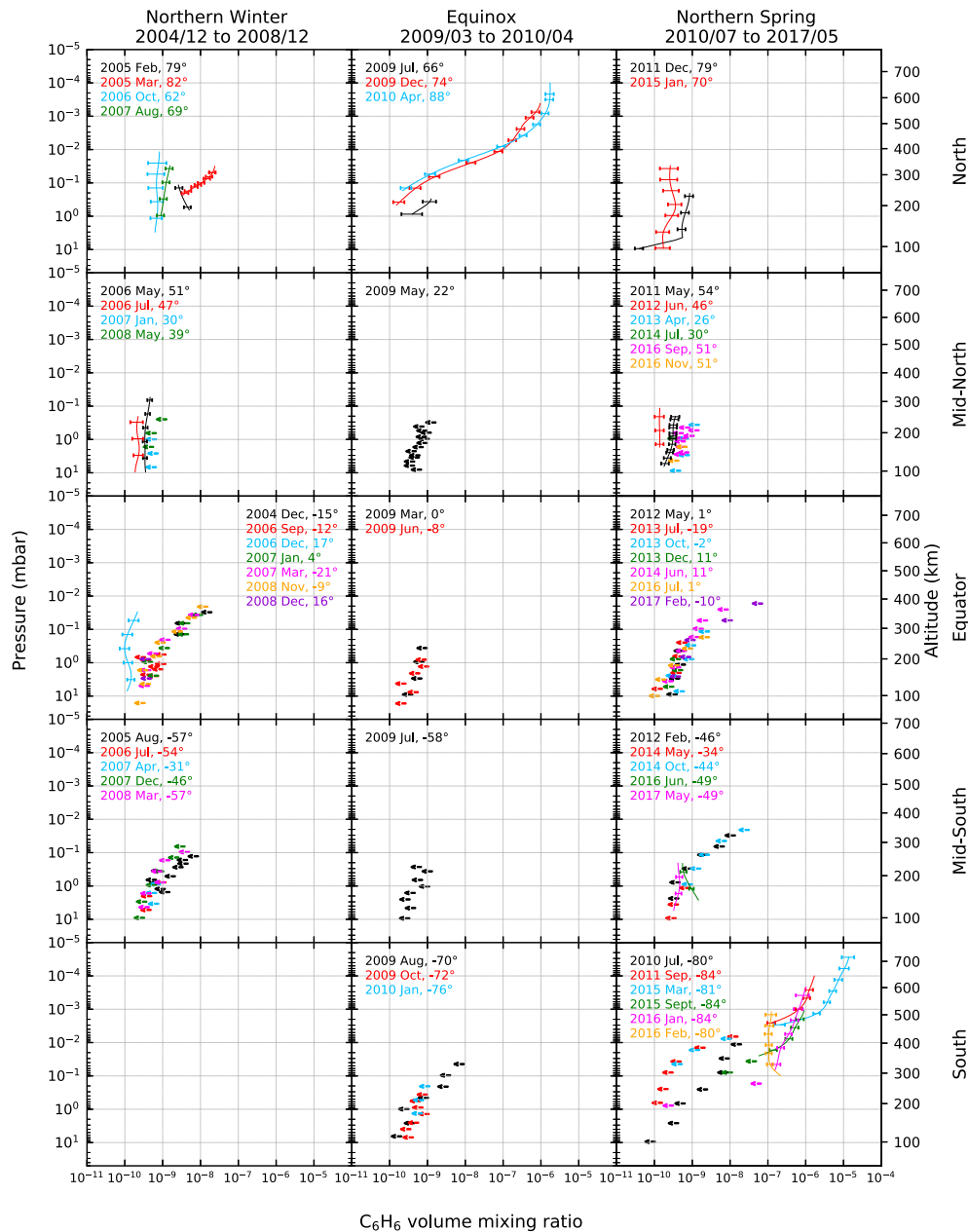
Fig. 11. C_6H_6 gas volume mixing ratio profiles in the middle atmosphere of Titan. Same format as Fig. 3.

December 2004, which is consistent with previous analyses of CIRS observations (Achterberg et al., 2011; Vinatier et al., 2015) and GCM predictions (Lebonnois et al., 2012; Lora et al., 2015; Newman et al., 2011; Vatant d'Ollone et al., 2018, in prep.). Below the 3×10^{-3} mbar pressure level (~480 km), we also observed an enrichment in all molecules, except CO_2, compared to their abundances around the equator, in agreement with the results of Vinatier et al. (2015), Teanby et al. (2019) and Sylvestre et al. (2018). This enrichment vastly differs from one compound to another. In the stratosphere, below the 0.1-mbar region, it is most marked for HC_3N, C_6H_6, C_4H_2, C_3H_4 and HCN, intermediate for C_2H_2, and weak for C_2H_6 and C_3H_8. From the GCMs predictions, the descending air branch of the pole-to-pole circulation cell brings air enriched in photochemical species from the high atmosphere and heats adiabatically the mesosphere, resulting in a temperature local maximum around 0.01 mbar (~410 km), instead of 0.1 mbar (~275 km) for the stratopause in the equatorial region. Below 0.3 mbar (~230 km), the temperature profile in the northern polar region is colder than around

the equator (by ~20 K at 1 mbar, ~175 km), in agreement with the results of Vinatier et al. (2015), Achterberg et al. (2011) and Teanby et al. (2019). The smaller stratospheric polar temperatures likely result from the absence of solar heating in the polar night below 300 km.

Between February 2005 and August 2007, we observed a decrease of the temperature of the polar stratopause by ~7 K at 0.01 mbar (~410 km), consistent with previous CIRS observations (Achterberg et al., 2011; Vinatier et al., 2015). This cooling could be due to the weakening of the descending branch of the pole-to-pole circulation cell at the end of winter. This assumption is supported by the decreasing speed of zonal winds around the northern polar region inferred by Achterberg et al. (2011) and predicted by GCMs (Lebonnois et al., 2012; Lora et al., 2015; Newman et al., 2011; Tokano, 2013; Vatant d'Ollone et al., 2018, in prep.). The temperature profiles in the lower stratosphere below 0.3 mbar (~230 km) did not vary between 2005 and 2007.

From August 2007 to July 2009, the stratopause temperature decreased by ~21 K at 0.01 mbar (~375 km), which is consistent with
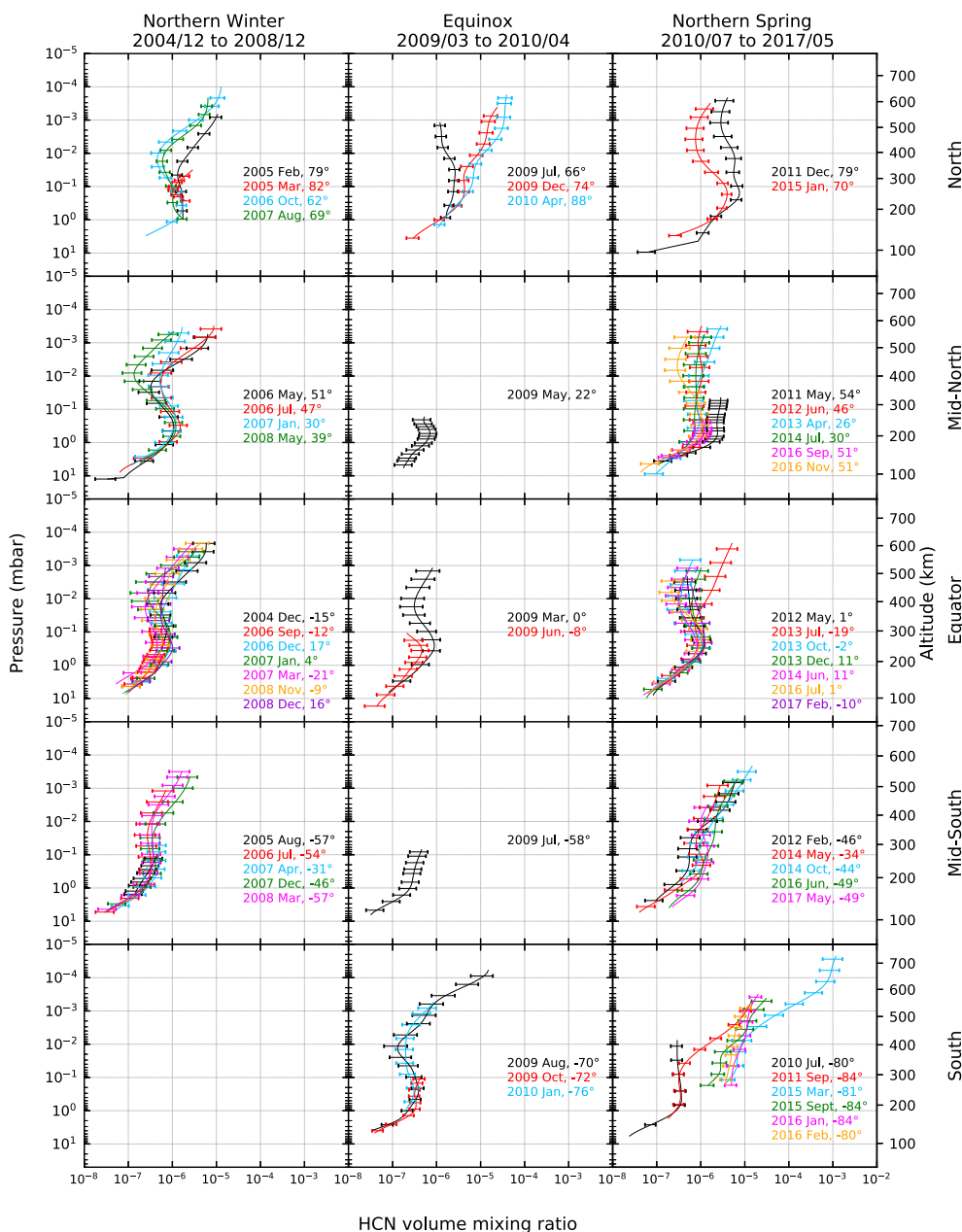
Fig. 12. HCN gas volume mixing ratio profiles in the middle atmosphere of Titan. Same format as Fig. 3.

previous analyses of CIRS observations (Achterberg et al., 2011; Vinatier et al., 2015). This trend is not reproduced by Newman et al.'s (2011) GCM which predicts warmer temperatures (in excess of 210 K) between 0.1 and 0.01 mbar at the northern spring equinox (11 August 2009) compared with the northern winter solstice (23 October 2002). The Vatant d'Ollone et al. (2018) (in prep.) GCM predicts this decreasing temperature trend, but with an amplitude at 0.01 mbar smaller by 10 K than what we derived. This cooling could be explained by the weakness of the adiabatic heating associated with downwelling motion because of the coexistence of two weaker equator-to-pole circulation cells that is predicted to occur around northern spring equinox (Lebonnois et al., 2012; Lora et al., 2015; Newman et al., 2011; Tokano, 2013; Vatant d'Ollone et al., 2018, in prep.). The lower stratosphere is still colder than at the equator because of the smaller solar flux at low altitudes. In December 2009, we observed an oscillation on the thermal profile that we discuss further in Section 5.3. In April 2010, the retrieved profile shows temperatures between 1 mbar (~160 km) and 0.01 mbar

(~360 km) lower than in July 2009, but this difference is possibly due to their different latitudes (89 and 67°). Regarding abundance profiles around the northern spring equinox, we observed a strong enrichment in photochemical compounds above 0.1 mbar (~250 km) compared to earlier during winter (Fig. 14). This enrichment in the mesosphere could be due to a combination of the reactivation of the photochemistry in the northern polar region by the increasing solar flux at altitudes higher than 500 km (Lebonnois et al., 2001), and the transport of this enriched air to deeper altitudes by the descending branch of the equator-to-pole circulation cell.

From April 2010 to December 2011, we observed a cooling above ~ 10^{-2} mbar (~450 km) and a slight heating below this pressure level consistent with Vinatier et al. (2015) and Teanby et al. (2019). Moreover, abundance profiles in December 2011 show a depletion in all molecules above 0.1 mbar (~260 km) compared to April 2010, as previously noted by Vinatier et al. (2015). This cooling and depletion in the mesosphere could be explained by the establishment of a pole-to-pole
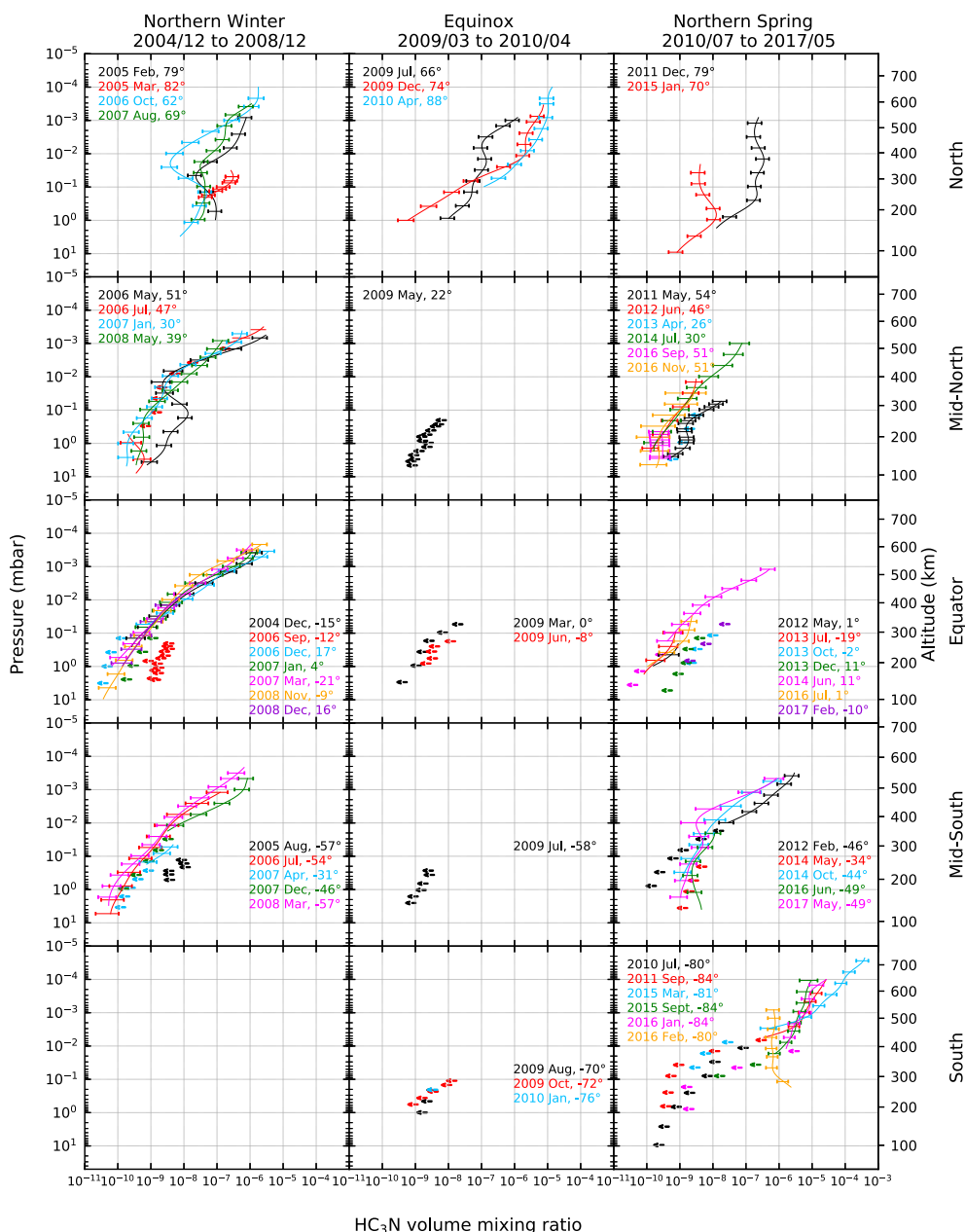
Fig. 13. HC$_3$N gas volume mixing ratio profiles in the middle atmosphere of Titan. Same format as Fig. 3.

circulation cell during the northern spring, in which the ascending branch occurs in the northern polar region, as predicted by GCMs (Lebonnois et al., 2012, Lora et al., 2015, Newman et al., 2011, Tokano, 2013, Vatant d'Ollone et al., 2018, in prep.). In contrast, the lower stratosphere warmed up probably due to the increasing solar flux in the northern polar region. Later in January 2015, the temperature profile had warmed up between 10 mbar (~100 km) and 0.03 mbar (~340 km), with an increase of ~9 K at 1 mbar (~175 km) and ~20 K at 0.1 mbar (~280 km), consistent with Coustenis et al.'s (2016) conclusions. This warming is reproduced by Newman et al.'s (2011) GCM, which predicts a temperature change at 1 mbar between the northern spring equinox and summer solstice consistent with the observations. However, at 0.1 mbar, the observed 20 K decrease is not reproduced by Newman et al.'s (2011) GCM. The stratospheric heating could be explained by the increasing solar flux reaching the northern polar region. Above 0.03 mbar, the temperature in the mesosphere did not vary between December 2011 and January 2015. In contrast, the abundances of all

molecules above 0.1 mbar (~280 km), except C$_2$H$_6$ and C$_3$H$_8$, decreased over this period, which is consistent with the upwelling provided by the pole-to-pole circulation cell. Actually, Vinatier et al. (in preparation) show that the depleted air is observed down to mid-northern latitudes. Surprisingly, the enrichment in photochemical compounds observed in December 2011 between 1 mbar (~175 km) and 0.1 mbar (~280 km) was still there in January 2015. This could be explained by the persistence of a circulation cell derived from the northern winter pole-to-pole circulation but confined to the stratosphere and to high northern latitudes as seen in the numerical simulation of Lebonnois et al. (2012) (see Fig. 12 of Sylvestre et al., 2018).

5.2.2. Southern polar region

We discuss here the evolution of the southern polar region starting in 2009 around the northern spring equinox, since there were no limb data acquired at high southern latitudes in the 2005–2008 period, during the northern winter.
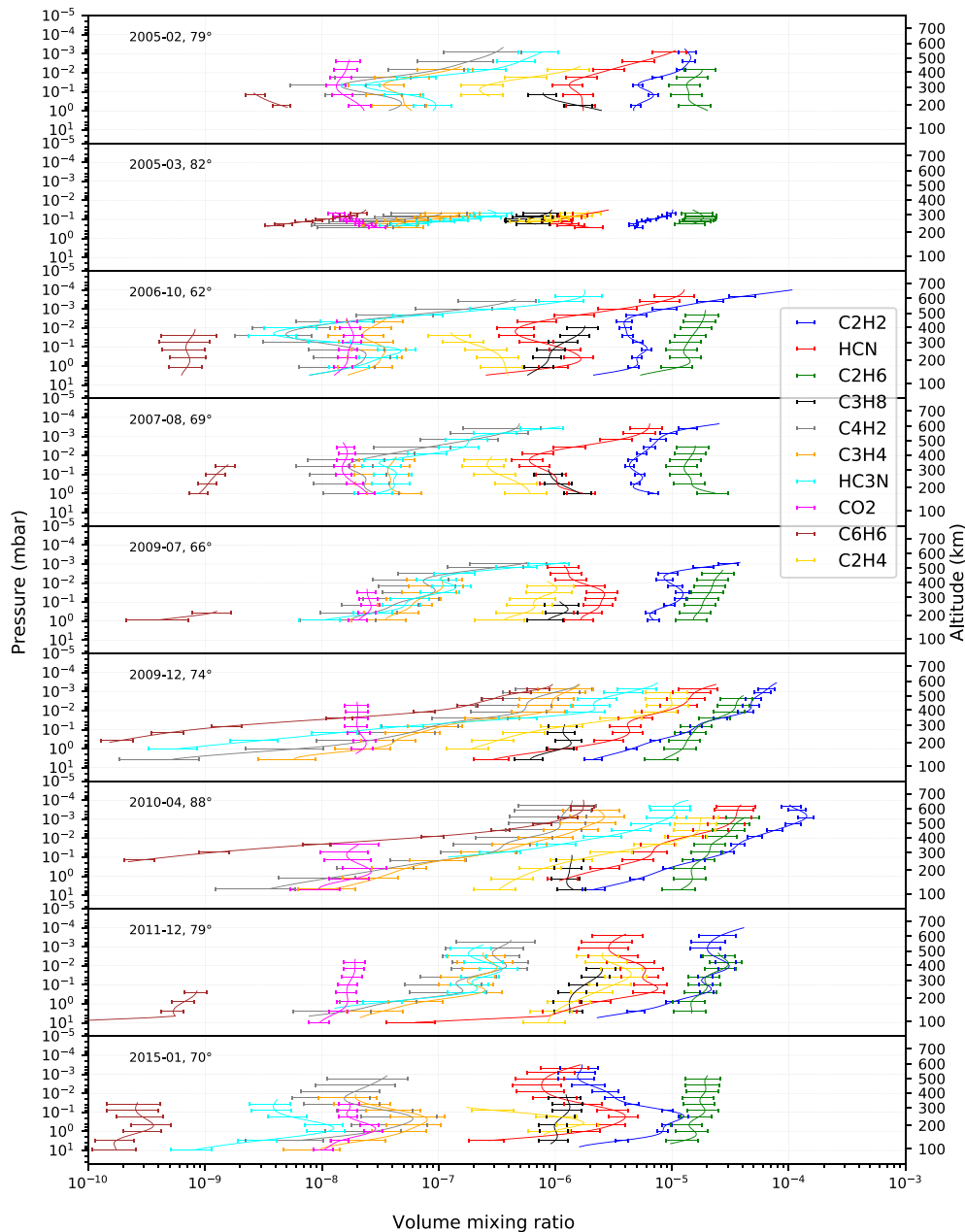
Fig. 14. Gas volume mixing ratio profiles from February 2005 to January 2015 in the northern polar region. The altitude scale corresponds to the October 2006 observations.

In August 2009, the thermal profile in the southern polar region is similar to the one around the equator in March 2009 between 0.3 mbar (~240 km) and 0.02 mbar (~370 km), as also derived by Vinatier et al. (2015), Achterberg et al. (2011), Teanby et al. (2012) and Teanby et al. (2017). This similarity is reproduced by Tokano's (2013) and Vatant d'Ollone et al.'s (2018) (in prep.) GCM, while Newman et al.'s (2011) GCM predicts a ~20 K higher temperature in the southern polar region. Below 0.3 mbar (~240 km), the thermal profile in the southern polar region is colder than the one around the equator (i.e: 5 K at 1 mbar, ~185 km), consistent with the results of Vinatier et al. (2015), Achterberg et al. (2011), and Teanby et al. (2019) and roughly with predictions of Newman et al.'s (2011) GCM and Vatant d'Ollone et al.'s (2018) (in prep.) GCM. Tokano's (2013) GCM does not predict such cooling between the equatorial region and the southern polar region near the northern spring equinox. Above 0.02 mbar (~370 km), mesospheric temperatures are warmer in the southern polar region than around the

equator (by ~10 K at~2 × 10^{-3} mbar, ~480 km). This could result from adiabatic heating in the descending branch of the equator-to-pole circulation cell, as seen in the northern polar region during the northern winter. However, this heating term is weak due to the coexistence of the two equator-to-pole circulation cells predicted by GCMs (Lebonnois et al., 2012; Lora et al., 2015; Newman et al., 2011; Tokano, 2013; Vatant d'Ollone et al., 2018, in prep.). In August 2009, C_2H_2 and HCN abundance profiles in the southern polar region are enriched above 0.001 mbar (~520 km) and 0.01 mbar (~400 km), respectively (Fig. 15) compared to the equatorial region. These enrichments in the mesosphere are due to the descending branch of the equator-to-pole circulation cell. Later in July 2010, the temperature in the southern polar region above 0.03 mbar (~455 km) increased by ~10 K, and cooled between 10 mbar (~95 km) and 0.03 mbar, with a ~8 K decrease at 0.2 mbar (~255 km). While the mesosphere was probably heated by the adiabatic compression occurring in the descending branch of the
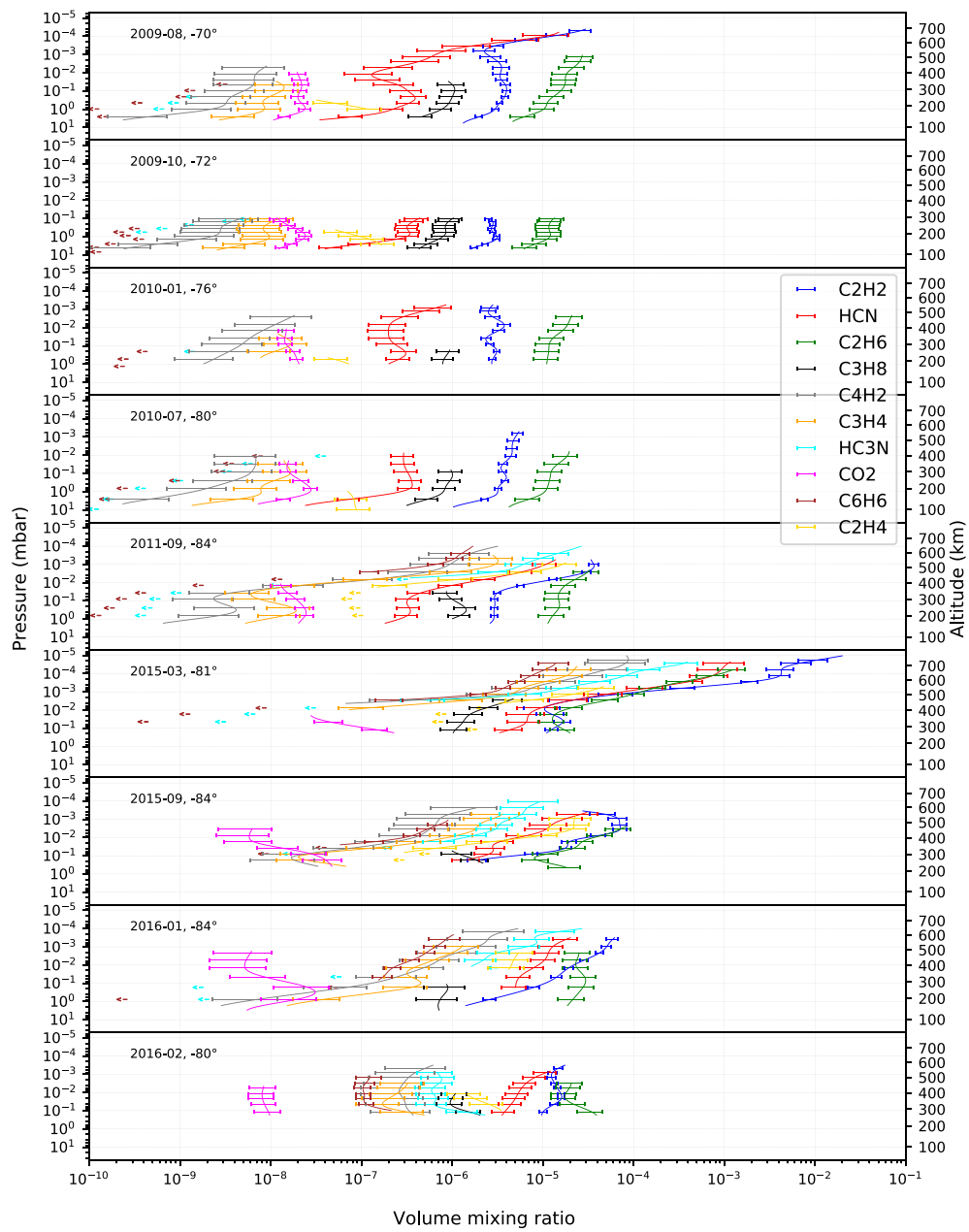
Fig. 15. Gas volume mixing ratio profiles from August 2009 to February 2016 in the southern polar region. The altitude scale corresponds to the October 2009 observations.

equator-to-pole circulation cell, the stratosphere most probably cooled due to the decreasing solar flux.

In September 2011, the temperature in the southern polar region increased in the mesosphere between 0.08 mbar (~280 km) and 4×10^{-3} mbar (~420 km) (by ~7 K at 0.01 mbar, ~380 km), while below 0.08 mbar the atmosphere strongly cooled, by ~16 K at 1 mbar (~175 km), in agreement with the CIRS data retrievals of Vinatier et al. (2015), Coustenis et al. (2016) and Teanby et al. (2017). The increasing temperature in the mesosphere is not reproduced by Vatant d'Ollone et al.'s (2018) (in prep.) GCM. At this date, all photochemical compound abundance profiles show mesospheric enhancements (see Fig. 14) compared to abundance profiles in July 2010, consistent with results of Vinatier et al. (2015) and Teanby et al. (2017). Additionally, C_6H_6 and HC_3N appeared for the first time in the southern polar region in September 2011. At this date, this suggests that the pole-to-pole circulation cell is well established in the middle atmosphere, since we observed in the southern polar region enrichment in photochemical compounds and warm temperature in the mesosphere, consistent with Teanby et al. (2017).

Between September 2011 and March 2015, the atmosphere in the southern polar region strongly cooled between 0.3 mbar (~210 km) and 4×10^{-4} mbar (~500 km) with a temperature decrease of ~26 K at 0.01 mbar (~350 km). This strong cooling of the middle atmosphere is consistent with the results of Coustenis et al. (2019) who inferred a steady decrease of temperature from June 2012 to September 2014 in the 0.01–20 mbar pressure range, and with Teanby et al.'s (2017) results. GCMs do not predict such a cooling in the mesosphere. Moreover, abundance profiles show a stronger enrichment in molecules above 0.01 mbar (~350 km) compared to September 2011 (Fig. 15). These profiles differ from those retrieved by Teanby et al. (2017) that show a local maximum in the C_2H_2 and C_3H_4 mole fractions around 440 km that we did not observe. Additionally, our C_2H_2, HCN, C_2H_6, HC_3N and C_6H_6 volume mixing ratios at 2×10^{-5} mbar (~645 km) are larger than those retrieved with INMS at 1050 km (Cui et al., 2009; Magee et al., 2009). However, Cui et al. (2009) and Magee et al. (2009) have analyzed INMS data during the northern winter (2004–2008) and primarily in the northern hemisphere, so the comparison with CIRS must be taken with caution. According to Teanby et al. (2017), the enrichment in short lifetime molecules (e.g., C_3H_4, C_4H_2, HC_3N and C_6H_6) in the mesosphere strongly increased the efficiency of the long-wave radiative cooling between September 2011 and March 2015, which is consistent with our derived abundance and temperature profiles. This is also consistent with the HCN cloud observed by VIMS in May 2012 at 300 km in the southern polar region that required temperatures close to 125 K to allow HCN to condense (De Kok et al., 2014). A polar cloud was also simultaneously observed by Cassini/ISS (West et al., 2016). In July 2012, CIRS observed an emission feature at 220 cm^{-1} attributed to a condensate (Jennings et al., 2012), and in May 2013, C_6H_6 ice was observed below 300 km by Vinatier et al. (2018).

From March to September 2015, the southern polar atmosphere strongly warmed up between 0.2 mbar (~215 km) and 10^{-4} mbar (~600 km), e.g. by ~31 K at 0.04 mbar (~285 km), as also observed by Teanby et al. (2017). Over the same period, abundance profiles show a decrease above 10^{-3} mbar (see Fig. 15), consistent with Teanby et al.'s (2017) observations. However, the lower stratosphere in the southern polar region is more enriched in trace gases than the equator, in agreement with the results of Sylvestre et al. (2018). According to Teanby et al. (2017), the re-appearance of a hot mesosphere is the result of the stabilization of the polar vortex with a slight reduction of the abundance of photochemical compounds, consistent with our observations (Fig. 15), and the adiabatic heating term outstripping the radiative cooling.

Between September 2015 and January/February 2016, the atmosphere in the southern polar region strongly cooled down below 0.01 mbar (~325 km), e.g. by ~30 K at 0.2 mbar (~210 km), in agreement with Teanby et al.'s (2017) results. This stratospheric cooling is

likely due to the lack of solar flux in this region and the relative weakness of the adiabatic heating as pressure increases. These thermal profiles show a colder stratopause than those observed in the northern polar region during the winter in 2005. Abundance profiles in January 2016 are similar to those in September 2015 between 0.1 mbar (~230 km) and 10^{-4} mbar (~565 km), consistent with Teanby et al.'s (2017) results, while between January and February 2016 abundance profiles have become relatively constant with altitude.

Between October 2014 and June 2016 at 51°S, the mesosphere above 0.04 mbar (~310 km) significantly warmed up (by ~11 K at 0.01 mbar, ~375 km) while the atmosphere below the 0.04-mbar region cooled down by 1–2 K. This mesospheric heating could be explained by an increase of the adiabatic heating in the descending branch of the pole-to-pole circulation cell. Teanby et al. (2017) suggested that the southern polar vortex was extending to ~ 60°S in 2016, which is consistent with our observations.

5.3. Thermal oscillation in the northern mesosphere near equinox

The thermal profile at 74°N in December 2009 shows an oscillation between 5×10^{-2} and 10^{-3} mbar (~300 and ~500 km) with a peak-to-peak amplitude of 3–4 K. We present here a possible explanation of this thermal oscillation. To do so, we re-analyzed the limb spectra recorded on 28 December 2009 (local time: 12 a.m., longitude: 255°W) at 0.5-cm^{-1} spectral resolution. We split the dataset in two subsets separated by around 6000 s, to search for a possible vertical displacement between the two retrieved thermal profiles. We also analyzed limb spectra recorded at 15.5-cm^{-1} spectral resolution on 11 December 2009 (local time: 9 p.m., longitude: 106°W) at 73°N and 78°N, in order to check if the oscillation was also present at a prior date. From these different datasets of limb spectra, we retrieved thermal profiles with the same methodology and the same a priori profile for each retrieval. In Fig. 16, we show thermal profiles retrieved from limb spectra at 0.5-cm^{-1} spectral resolution (blue and cyan) and 15.5-cm^{-1} spectral resolution at 73°N and 78°N (orange and red respectively). We conclude that the oscillation persisted at least during 6000 s on 28 December 2009, while
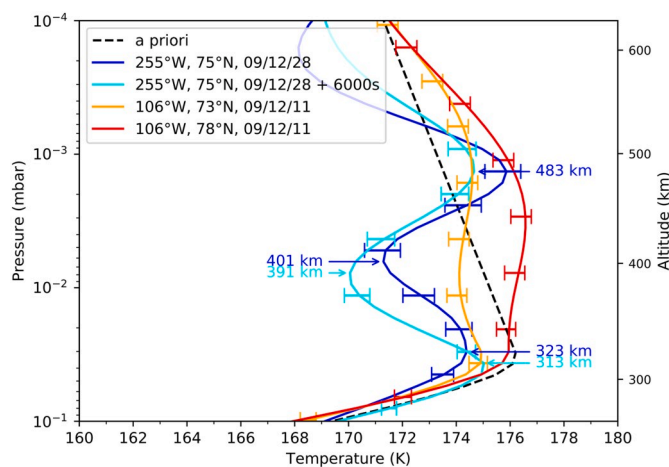
Fig. 16. Temperature profiles retrieved on 11 and 28 December 2009: blue and cyan thermal profiles retrieved from spectra recorded at 0.5-cm^{-1} spectral resolution on 28 December 2009 (local time: 12 a.m.), longitude 255°W, latitude 75°N and spaced in time by 6000 s respectively; orange and red thermal profiles retrieved from spectra recorded at 15.5-cm^{-1} spectral resolution on 11 December 2009 (local time: 9 p.m.), longitude 106°W, latitude 73°N and 78°N respectively. The dashed line is the a priori temperature profile used in all retrievals. (For interpretation of the references to color in this figure legend, the reader is referred to the web version of this article.)

one Titan day before, the atmosphere did not present such an oscillation at a location close in latitude.

Let's assume that this oscillation results from an atmospheric wave. From Fig. 16, we estimate that the wave moved in phase by $\sim$-10 $\pm$ 20 km in 6000 s (we are confident about the error bar, which corresponds to half of the altitude gap between two limb spectra), giving a phase speed c_z in the range -5 and $+1.7 \, \text{m s}^{-1}$. We can also measure a vertical wavelength $L_z \sim 170$ km between 5×10^{-2} mbar ($\sim$300 km) and 10^{-3} mbar ($\sim$500 km).

We determined the type of wave that verifies the above characteristics and fulfills the required criteria among six different types of waves in a cyclostrophic regime according to Peralta et al. (2014a) and Peralta et al. (2014b). We found that an inertia-gravity wave is relevant to our case. The general dispersion relation is given by:

$$\omega = \pm \sqrt{\frac{N_B^2 k_x^2 + \xi^2 \left(m^2 + \frac{1}{4H_0^2}\right)}{k_x^2 + m^2 + \frac{1}{4H_0^2}}} + k_x u_0 \quad (3)$$

where N_B is the Brunt-Väisälä frequency ($\sim 2.4 \times 10^{-3} \, \text{s}^{-1}$ at 400 km), k_x is the horizontal wavenumber, m is the vertical wavenumber, H_0 is the pressure scale height ($\sim$50 km at 400 km), u_0 is the zonal wind (65 $\pm$ 15 m s^{-1} at 74°N and 400 km as retrieved by Achterberg et al. (2011) in 2009), and ξ is a frequency defined as:

$$\xi^2 = 2\psi\left(\psi - \frac{1}{a+z}\frac{\partial u_0}{\partial \phi}\right) \quad (4)$$

where a is Titan's radius, z the altitude (400 km), ϕ is the latitude and ψ is the centrifugal frequency defined as:

$$\psi = \frac{u_0}{a+z}\tan(\phi) \quad (5)$$

We evaluated the meridional shear of the zonal wind $\partial u_0 / \partial \phi$ from the map of Achterberg et al. (2011) showing a $-40 \, \text{m s}^{-1}$ variation from 69°N to 76°N in 2009, and found that $\xi \sim 1.7 \times 10^{-4} \, \text{s}^{-1}$. We find that for any horizontal wavenumber ($k_x = 2\pi n/L_x$, where L_x is the perimeter of the latitude circle at 74°N and 400 km, and n a positive integer), one of the two solutions of Eq. (3) yields a vertical phase velocity $c_z > 7 \, \text{m s}^{-1}$, which is excluded by our observations. For $n \leq 10$, the other solution yields c_z between 1.3 and $-3 \, \text{m s}^{-1}$, which is consistent with our observations. For $n > 10$, the solutions are not consistent with our constraints on the phase velocity. Note that for these solutions the vertical group velocity as derived from Eq. (3) is positive given that $\xi < N_B$, which means that energy is propagating upwards. Their horizontal phase velocity c_k varies between -87 (for $n=1$) and $+4 \, \text{m s}^{-1}$ (for $n=10$), smaller than the zonal wind $u_0 = 65 \, \text{m s}^{-1}$. For $n \leq 6$, the wave phase moves westwards. The corresponding period ($2\pi/\omega$) is at least 17 h. These inertia-gravity waves verify the criteria of Peralta et al. (2014a): (1) ξ^2 varies by less than a factor of 2 over a reasonable latitude range around 74°N, e.g. 70°N and 80°N, (2) the intrinsic horizontal phase velocity $|\overline{c_k}| = |c_k - u_0| = |\frac{\overline{w}}{k_x}|$ is higher than $\lambda_z \times \partial u_0 / \partial z$ ($\sim$50 m s^{-1}) for $n \leq 10$.

This oscillation could thus be explained by an inertia-gravity wave, but the mechanism needed to produce the wave is unknown. As the wave energy is propagating upwards, it could be generated from convection in the troposphere, possibly due to some instability occurring around equinox.

If the oscillating structure of the 74°N temperature profiles is not due

to a wave, it could have a radiative origin, such as localized haze layers producing enhanced heating or a photochemically-enriched layer around 10^{-2} mbar ($\sim$300 km) that would enhance the radiative cooling. However, the haze extinction profile we simultaneously retrieved did not present significant variations that could be linked to detached haze layers. Also, the molecular abundance profiles we retrieved are relatively uniform around 10^{-2} mbar ($\sim$300 km) where the local minimum in temperature is located. We therefore discard a purely radiative origin for the observed oscillation.

6. Conclusion

The CIRS limb observations acquired at 0.5-cm^{-1} spectral resolution have allowed us to monitor seasonal changes of temperature and abundance profiles in the middle atmosphere of Titan from 2004 to 2017, i.e. over almost half a Saturnian year. Using the latest calibration version and a new methodology to average limb spectra, we got a better signal-to-noise ratio on limb spectra that allowed us to probe higher altitudes ($\sim$ 650 km) than previous CIRS analyses (Teanby et al., 2017; Vinatier et al., 2015). Our study is consistent with Vinatier et al.'s (2015) work between 2006 and 2012 and Coustenis et al.'s (2019), and Teanby et al.'s (2019) results inferred from analysis of CIRS nadir spectra. All vertical profiles displayed in this paper are available as supplementary material and can be downloaded from the VESPA data portal (Virtual European Solar and Planetary Access, http://vespa.obspm.fr/planet ary/data/). We summarize below some important results:

- During the northern winter, in the northern polar region, we observed temperatures in the mesosphere above 0.1 mbar ($\sim$175 km) that are much larger than at equatorial latitudes in the period 2005–2007 (northern winter). This is likely due to compressional heating occurring in the descending branch of a global circulation cell. It results in a stratopause located around 0.01 mbar ($\sim$410 km), one pressure decade above that around the equator (0.1 mbar, $\sim$275 km). Downwelling also explains the large enrichment in most photochemical compounds compared to equatorial and mid-latitudes, particularly in the stratosphere below the 0.1-mbar region. The enrichment varies from one species to another, being huge for molecules like HC_3N, C_6H_6, C_4H_2, C_3H_4 and HCN, and weak to inexistent for C_2H_6, C_3H_8, and CO_2. In 2009–2010, shortly after the equinox, we derived a strong enrichment in all molecules above the 0.1-mbar ($\sim$250 km) region compared to winter conditions, a possible consequence of the increasing solar flux and local photochemical production. Simultaneously, the atmosphere cooled in the whole 1–0.001 mbar region ($\sim$165–495 km). A year or so later, in December 2011, the atmosphere had cooled above 0.03 mbar ($\sim$320 km) but warmed up below 0.03 mbar, probably due to the increase of solar flux. Till January 2015, temperature continued to increase below 0.03 mbar ($\sim$340 km), yielding a stratopause located at 0.1 mbar ($\sim$280 km), similar to its location in the equatorial region.
- During northern spring at high northern latitudes, the enrichment in all photochemical species in the range 1–0.1 mbar ($\sim$175-280 km) persisted from December 2011 to January 2015, possibly due to a residual circulation cell as predicted by Lebonnois et al.'s (2012) General Circulation Model (see Fig. 12 of Sylvestre et al., 2018).
- The southern polar region underwent strong seasonal changes in temperature and abundance profiles from July 2010 to January 2016. From July 2010 to September 2011, the atmosphere below

0.1 mbar (~280 km) cooled down, likely in response to the decreasing solar flux. From September 2011 to March 2015, the atmosphere in the region 0.2 –4 × 10^{-4} mbar (~225–500 km) strongly cooled down, at least partly because of the strong enrichment in photochemical compounds above 0.01 mbar (~350 km), which increases the efficiency of the radiative cooling (Teanby et al., 2017). Additionally, the mixing ratios we retrieved in March 2015 are larger at 2 × 10^{-5} mbar (~645 km) than those measured *in situ* with the INMS at 1050 km (Cui et al., 2009; Magee et al., 2009). Later, in September 2015, we observed that the temperature had increased between 0.2 mbar (~215 km) and 10^{-4} mbar (~600 km). According to Teanby et al. (2017), this is a result of the slight reduction in infrared-active compounds and the strengthening of the pole-to-pole circulation, which allows the adiabatic heating of the descending branch to outstrip the thermal emission cooling. In January 2016, the temperatures below 0.01 mbar (~325 km) are much lower than in September 2015, probably due to the lack of solar flux. In June 2016, we see that the polar vortex, characterized by an enrichment of the photochemical species, was extending equatorward down to ~ 50°S.

- The equatorial latitudes present weak seasonal variations of thermal and abundance profiles from the northern winter to the northern spring. We note that equatorial CO_2 abundance profiles show a local maximum at 1 mbar (~188 km) and a local minimum near 0.1 mbar (~290 km) that are not predicted by photochemical models (Dobrijevic et al., 2016; Krasnopolsky, 2014; Loison et al., 2015; Vuitton et al., 2019). We have been able to detect HC_3N at equatorial latitudes at altitudes as high as ~580 km (3 × 10^{-4} mbar) with an abundance of a few ppmv, consistent with UVIS stellar occultation retrievals at 550 km (Koskinen et al., 2011).
- An oscillation of the thermal profile between 300 and 500 km has been observed in December 2009 at 74°N. Its characteristics (vertical wavelength and weak vertical phase velocity) are consistent with an inertia-gravity wave, given the estimated zonal wind and meridional shear at this latitude and time.

To conclude, we have shown that the descending branch of the circulation cell strongly impacts the thermal structure and abundances of photochemical products at high latitudes in the mesosphere and stratosphere. Comparing the evolution of both poles is difficult since the coverage by the Cassini mission is not symmetric in season. Moreover, the north pole in winter is 1 AU closer to the Sun than the south pole in winter due to Saturn's eccentricity. This asymmetry in the insolation pattern may lead to an asymmetry in the dynamics at high latitudes. Unfortunately, the southern pole, presently in the polar night, cannot be observed from ground-based facilities such as ALMA (Cordiner et al., 2018; Thelen et al., 2019) but we can still study the evolution of the north pole during the northern summer, in order to compare with the south pole at a similar season.

Acknowledgments

Appendix A. List of observations

Table 1
List of limb observations used in this study.

Flyby	Date	Solar longitude (°)	Solar zenith angle (°)	Local time (hh:mm)	Latitude FP3 (°N)	Longitude FP3 (°W)	Vertical resolution (km) (see Appendix B)	Altitude shift applied for each block 1/2/3/4 (km)
90° N-60° N								
T3	14 Feb 2005	301	108	15:40	79	83	40	−10/−10/−10/−10/−10/−10/−10
T4	31 Mar 2005	303	107	08:10	82	137	10	30/4
T19	09 Oct 2006	324	117	19:50	62	270	40	67/50/53/45
T35	30 Aug 2007	335	92	16:10	69	102	40	−9/−9/−9/−9
T59	24 Jul 2009	359	68	13:12	66	307	40	23/23
T64	28 Dec 2009	5	73	12:00	74	262	40	−3/−10/−8/−12
T67	05 Apr 2010	8	87	1:00	88	204	40	9/2/4/0
T79	13 Dec 2011	28	77	17:35	79	100	40	−9/−11/−9/−9
T108	12 Jan 2015	64	47	12:45	70	338	40	13/5/13/13
60° N-20° N								
T14	20 May 2006	318	148	23:33	51	262	40	−19/−26/−19/−26
T16	21 Jul 2006	321	143	22:00	47	235	40	8/1
T24	29 Jan 2007	328	69	15:45	30	341	40	10/0/0/−5
T43	12 May 2008	344	60	14:38	39	141	40	11/11/1
T54	05 May 2009	357	95	18:20	22	231	10	−12/−12/−12/−12
T76	08 May 2011	21	110	2:20	54	75	10	18/18/13/13
T84	06 Jun 2012	34	77	6:17	46	281	40	10/5/10/5
T90	05 Apr 2013	44	100	4:40	26	271	40	−6/−9/−8/−9
T103	20 Jul 2014	58	67	7:00	30	91	40	−3/−13/−13/−13
T123	27 Sep 2016	83	45	8:33	51	80	10	−3

Table 1 (*continued*)

Flyby	Date	Solar longitude (°)	Solar zenith angle (°)	Local time (hh:mm)	Latitude FP3 (°N)	Longitude FP3 (°W)	Vertical resolution (km) (see Appendix B)	Altitude shift applied for each block 1/2/3/4 (km)
T125	30 Nov 2016	85	74	5:32	51	138	40	13/13/16/16
20 ° N–20 ° S								
Tb	13 Dec 2004	299	91	5:33	−15	260	40	28/33/33/33
T18	07 Sep 2006	322	32	9:48	−12	68	20	0/0/0/0
T21	12 Dec 2006	326	150	21:59	17	237	40	−3/−8/2/−6
T23	12 Jan 2007	327	21	11:21	4	33	40	7/2/7/2
T27	25 Mar 2007	330	55	15:48	−21	142	40	20/16/23/18
T47	19 Nov 2008	351	20	10:43	−9	179	40	8/2/2/−2
T49	21 Dec 2008	352	142	21:31	16	19	40	25/25/15
T51	21 Mar 2009	355	156	22:26	0	12	40	20/15/25/15
T57	22 Jun 2009	358	110	19:20	−8	213	20	7/7/7/12
T83	21 May 2012	34	89	17:55	1	115	40	36/33/35/30
T92	10 Jul 2013	47	172	00:34	−19	348	40	12/8/12/8
T95	14 Oct 2013	50	23	12:19	−2	188	40	6/3/6/−2
T96	01 Dec 2013	51	140	1:30	11	342	40	31/28/31/31
T102	18 Jun 2014	57	99	5:04	11	95	40	−13/−15/−22/−22
T121	25 Jul 2016	81	89	6:04	1	110	40	−19/−22/−14/−15
S98	17 Feb 2017	87	161	23:00	−10	213	115	11/16/21/31
20 ° S–60 ° S								
T6	22 Aug 2005	308	89	20:07	−57	308	10	−1
T15	02 Jul 2006	320	45	13:50	−54	281	40	5/2/5/2
T28	11 Apr 2007	330	74	6:45	−31	284	30	4
T39	21 Dec 2007	339	99	4:30	−46	286	40	13/7/12/4
T42	25 Mar 2008	343	92	4:55	−57	262	40	1/−9
T58	24 Jul 2009	359	108	20:25	−58	192	20	0/6/6/6
T82	18 Feb 2012	31	141	1:54	−46	56	40	1/−9/1/1
T101	17 May 2014	56	124	19:47	−34	253	40	23/18/23/21
T106	23 Oct 2014	61	124	19:40	−44	236	40	−27/−33/−24
T120	07 Jun 2016	79	137	3:07	−49	142	40	2/−5/−3/−4
T126	23 May 2017	90	128	20:00	−49	225	40	10/−10
60 ° S–90 ° S								
T61	25 Aug 2009	1	102	3:42	−70	84	40	33/23
T62	12 Oct 2009	2	88	17:28	−72	242	20	5/5/10/5
T65	12 Jan 2010	5	108	23:34	−76	61	40	−5/−7/−5/−7
T71	06 Jul 2010	11	103	2:15	−80	356	40	−19
T78	11 Sep 2011	25	98	14:40	−84	219	40	−1/−8/−4/−8
T110	16 Mar 2015	66	122	2:37	−81	137	40	108/108/108/82
T113	29 Sep 2015	72	113	15:40	−84	53	40	71/74/89
T115	31 Jan 2016	76	118	4:00	−84	135	40	−48/−18/−48/12
T117	16 Feb 2016	76	126	0:00	−80	196	40	−29/−39

Appendix B. Limb spectra averaging

During a given flyby, the CIRS instrument acquired a set of limb spectra in different altitude ranges during sequences that we call "blocks" (Fig. 17). In a block, each of the ten detectors recorded around 30 spectra at roughly the same altitude level, as the spacecraft was approaching or getting away from Titan. For each block, we first averaged spectra detector-by-detector.
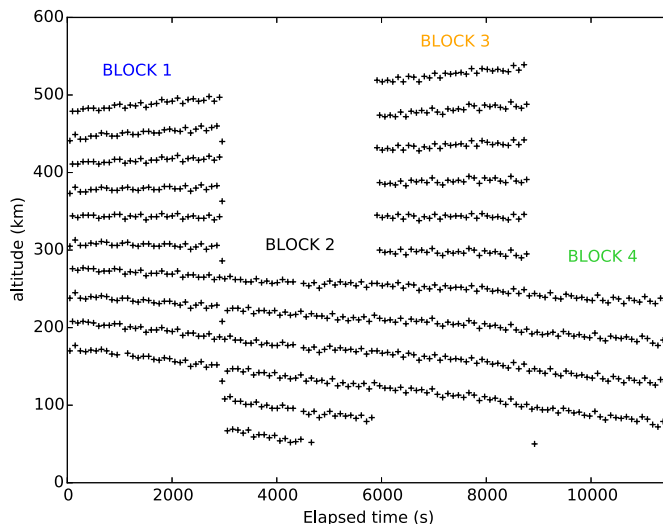

Fig. 17. Diagram of measurements performed by CIRS during the T64 flyby (Dec 2009, 74 °N). Each cross corresponds to a spectrum acquired at a given altitude (y-axis) and time (x-axis).

We considered the vertical profile of the spectral radiance in each block, using the ten (or less) available averaged spectra (Fig. 18). We integrated the radiance over the spectral range 1250–1350 cm^{-1} of the ν_4 band of methane, and altitudes were extracted from the CIRS database. Without instrument pointing error, we should observe a continuity of the radiance profile from one block to another. In fact, we noticed that, for some flybys, we needed to apply a relative altitude shift from one block to another. We used one of the two deepest blocks as a reference block (e.g. Block 2 in Fig. 17). The reference block is chosen based upon two criteria: (1) a medium vertical resolution and (2) one of the two deepest blocks since we determined the vertical shift from the fit of the P- and Q-branches of the ν_4 methane band in the deepest limb spectra (Section 3.1). Vertical shift adjustments relative to the pointing information in the CIRS database may originate from the pointing precision achieved through the momentum wheels of Cassini, which is about 4×10^{-5} rad (Flasar et al., 2004). For the limb observations used here, the spacecraft was usually at typically 150,000 km from Titan, which gives an error on altitude of about 6 km. In the case shown in Fig. 19, we needed to apply relative altitude shifts of about +7 km on Block 1, +2 km on Block 3 and −2 km on Block 4. These relative altitude shifts applied to the blocks are consistent with the spacecraft pointing precision. This is also the case for most of the blocks of limb spectra listed in Table 1 (last column). The total altitude shift of each block is the sum of this relative altitude shift and the shift derived from the fit of the P- and Q-branches of the ν_4 methane band described in Section 3.1. Based on the altitude of limb spectra in the reference block, we built an altitude grid with a step equal to the vertical resolution of the observation. Taking into account the relative altitude shift of each block, we linearly interpolated the spectra of each block over this grid and, at each point of the grid, calculated the mean of the interpolated values.
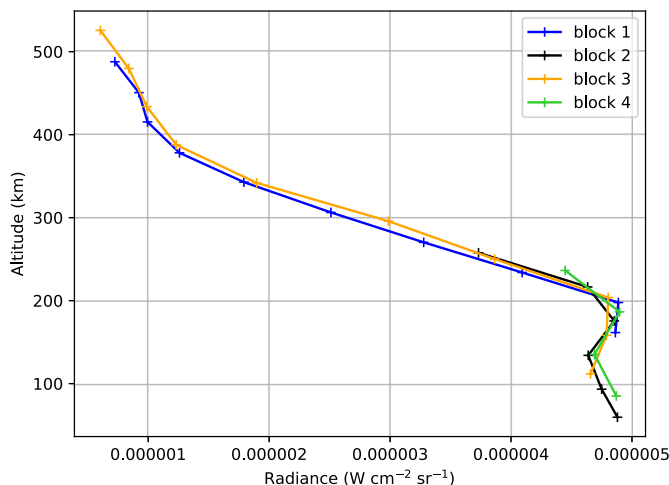

Fig. 18. Profiles of spectral radiance integrated over the spectral range 1250–1350 cm^{-1} for each block of data shown in Fig. 17. Each point corresponds to an averaged spectrum for one specific detector. Colors represent the different blocks used. (For interpretation of the references to color in this figure legend, the reader is referred to the web version of this article.)
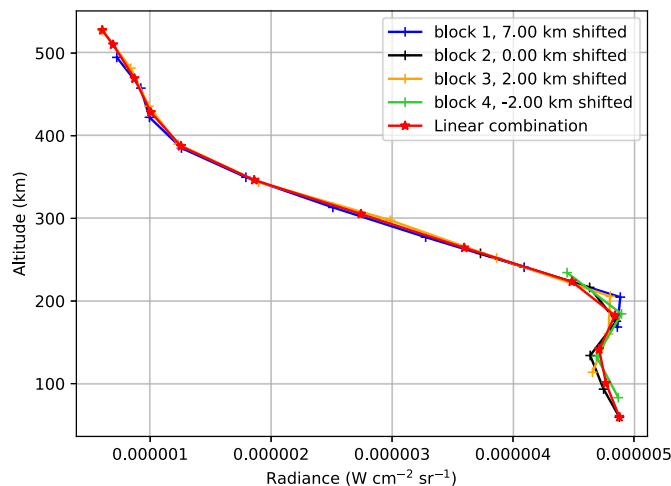
Fig. 19. Profiles of spectral radiance integrated over the spectral range 1250–1350 cm^{-1} after shifting Blocks 1, 3, 4 relatively to Block 2. Each point corresponds to an averaged spectrum for one specific detector. Colors represent the different blocks used. The red profile correspond to the linear combination of the radiances from all four blocks. (For interpretation of the references to color in this figure legend, the reader is referred to the web version of this article.)

Appendix C. Negative continuum correction

Some calibrated FP4 limb spectra show a negative continuum from 1075 to 1200 cm^{-1} at high altitudes ($\gtrsim$450 km) (see Fig. 20 in red) where the signal is low (SNR < 1). When selecting spectra from the database, we removed from the average the spectra showing by eye a negative continuum, referred hereafter as "corrupted" spectra. However, the averaged spectra we obtained still presented in a few cases a negative continuum, which leads to an underestimation of the retrieved temperature profile. This problem is mostly visible on T21 and T23 FP4 limb spectra. We tried an approach to correct the continuum in such averaged spectra and estimate the error propagation to the retrieved temperature profile.

In the simple case shown here, we extracted from the same block and detector two adjacent spectra: a correct spectrum (used as a reference), and a corrupted one (Fig. 20). The difference spectrum is close to 0 at 1500 cm^{-1} and shows a linear dependence with wavenumber. We therefore decided to add a linear radiance contribution to the corrupted spectrum. To do so, we defined on the corrupted spectrum three points. Point A, at x $_A = 1100$ cm^{-1}, is located in the spectral region that we usually use to retrieve the haze optical depth from the fit of the continuum. Radiance y$_A$ corresponds to the radiance averaged between 1080 and 1120 cm^{-1}. Point B is located at x $_B = 1415$ cm^{-1}, between the R branch of the CH$_4$ ν_4 band and the C$_2$H$_6$ ν_7 band, and y$_B$ corresponds to the averaged radiance between 1406 and 1424 cm^{-1}. Point C is located at x $_C = 1487$ cm^{-1}, close to the edge of the spectrum.

The linear radiance correction δy that we added to the corrupted spectrum is:

$$\delta y = \frac{y_A - y_B}{x_B - x_A} * (x - x_C) \tag{1}$$

The corrected spectrum is then:

$$I_{corrected} = I_{corrupted} + \delta y \tag{2}$$

We added the radiance correction from Eq. (1) to any averaged spectrum in which the continuum appeared to be negative beyond the noise level (only for flyby T21 and T23). This empirical procedure satisfactorily removes the negative continuum but may be not optimal as the distortion of the continuum may differ from the linear trend given by Eq. (1) which was based on a single case.
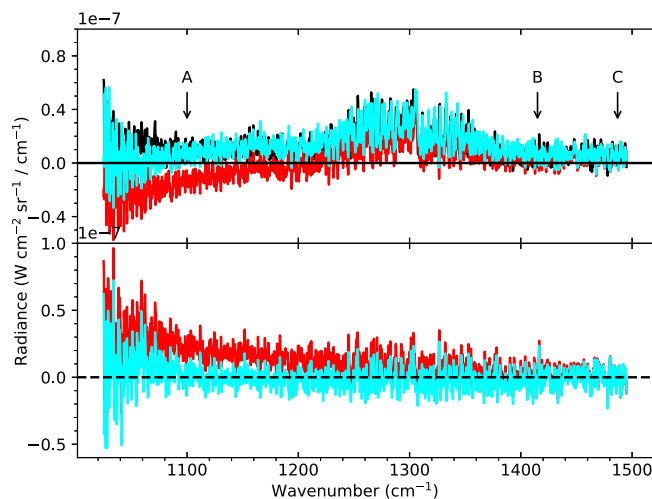
Fig. 20. Top panel: a spectrum used as a reference (black) and a corrupted spectrum (red) extracted from Detector 30 in Block 1 of Flyby T71. After the correction procedure, we obtain the spectrum shown in blue. Bottom panel: residuals between *i)* the reference spectrum and the corrupted spectrum (red), and *ii)* the reference spectrum and the corrected spectrum (blue). (For interpretation of the references to color in this figure legend, the reader is referred to the web version of this article.)

Appendix D. Influence of the methane abundance on the retrievals

Our hypothesis of a constant methane mixing ratio in the stratosphere at all latitudes may be questioned, considering the work of Lellouch et al. (2014). Analyzing Cassini/CIRS spectra of both the rotation and ν_4 methane bands, these authors derived latitudinal variations of the stratospheric CH_4 mixing ratio during the northern winter, ranging from 1% at the equator and 50–55° N and S to 1.5% at 30–35° N and S and at the poles. We investigated the influence of using 1% of methane (instead of 1.48%) on the temperature and molecular abundance profile retrievals. We selected the T49 flyby observations (December 2008, 16°N) and conducted the methodology previously used but with a CH_4 mixing ratio of 1% instead of 1.48%.

The retrieved temperature profile is at most 4 K warmer with 1% of methane in the stratosphere below the 0.1-mbar pressure level (~290 km). This warmer temperature profile impacts the retrieved abundance profiles, which are about 20% smaller than those retrieved with 1.48% (Fig. 21). We did not take into account this uncertainty on the molecular profiles displayed in Figs. 4– 13 as Lellouch et al. (2014) analysis is limited to the northern winter and the results may be different during the northern spring. We also chose to be consistent over our whole study in which all retrievals were performed with a uniform CH_4 mixing ratio of 1.48%. This investigation points out the importance of constraining the methane abundance profile as a function of location and season.
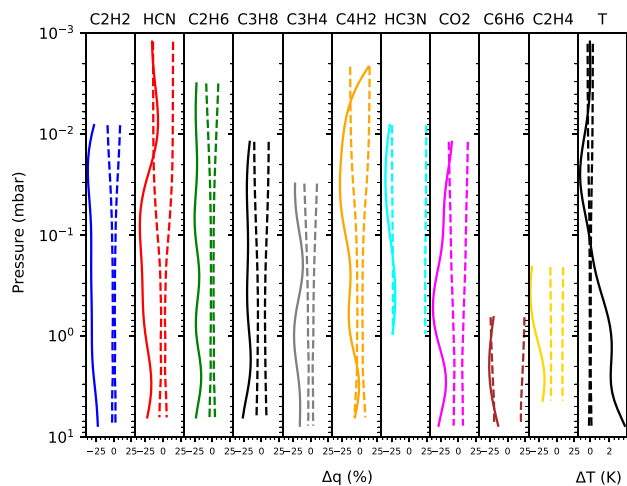

Fig. 21. Relative variation of the retrieved mixing ratio (%) and temperature (K) profiles corresponding to a change of the CH_4 mixing ratio above the troposphere from 1.48 % to 1.00% (solid lines). CIRS spectra recorded in December 2008 at 16°N were used for this test. Dashed lines correspond to the formal errors attached to the retrieved profiles with 1.48% of methane.

References

Achterberg, R.K., Conrath, B.J., Gierasch, P.J., Flasar, F.M., Nixon, C.A., 2008. Titan's middle-atmospheric temperatures and dynamics observed by the Cassini Composite Infrared Spectrometer. Icarus 194, 263–277. https://doi.org/10.1016/j.icarus.2007.09.029.

Achterberg, R.K., Gierasch, P.J., Conrath, B.J., Michael Flasar, F., Nixon, C.A., 2011. Temporal variations of Titan's middle-atmospheric temperatures from 2004 to 2009 observed by Cassini/CIRS. Icarus 211, 686–698. https://doi.org/10.1016/j.icarus.2010.08.009.

Bézard, B., Yelle, R.V., Nixon, C.A., 2014. The composition of Titan's atmosphere. In: Müller-Wodarg, I.C.F., Griffith, C.A., Lellouch, E., Cravens, T.E. (Eds.), Titan. Cambridge University Press, Cambridge, UK, p. 158. https://doi.org/10.1017/CBO9780511667398.008.

Brasunas, J.C., 2012. Laser mode behavior of the Cassini CIRS Fourier transform spectrometer at Saturn. Infrared Phys. Technol. 55, 533–537. https://doi.org/10.1016/j.infrared.2012.07.003.

Conrath, B.J., Gierasch, P.J., Ustinov, E.A., 1998. Thermal structure and para hydrogen fraction on the outer planets from Voyager IRIS measurements. Icarus 135, 501–517. https://doi.org/10.1006/icar.1998.6000.

Cordiner, M.A., Nixon, C.A., Charnley, S.B., Teanby, N.A., Molter, E.M., Kisiel, Z., Vuitton, V., 2018. Interferometric imaging of Titan's HC$_3$N, H^{13}CCCN and HCCC^{15}N. Astrophys. J. Lett. 859, L15. https://doi.org/10.3847/2041-8213/aac38d.

Coustenis, A., Jennings, D., Achterberg, R., Lavvas, P., Bampasidis, G., Nixon, C., Flasar, F., 2019. Titan's neutral atmosphere seasonal variations up to the end of the Cassini mission. Icarus 113413. https://doi.org/10.1016/j.icarus.2019.113413.

Coustenis, A., Jennings, D.E., Achterberg, R.K., Bampasidis, G., Lavvas, P., Nixon, C.A., Teanby, N.A., Anderson, C.M., Cottini, V., Flasar, F.M., 2016. Titan's temporal evolution in stratospheric trace gases near the poles. Icarus 270, 409–420. https://doi.org/10.1016/j.icarus.2015.08.027.

Crespin, A., Lebonnois, S., Vinatier, S., Bézard, B., Coustenis, A., Teanby, N.A., Achterberg, R.K., Rannou, P., Hourdin, F., 2008. Diagnostics of Titan's stratospheric dynamics using Cassini/CIRS data and the 2-dimensional IPSL circulation model. Icarus 197, 556–571. https://doi.org/10.1016/j.icarus.2008.05.010.

Cui, J., Yelle, R.V., Vuitton, V., Waite, J.H., Kasprzak, W.T., Gell, D.A., Niemann, H.B., Müller-Wodarg, I.C.F., Borggren, N., Fletcher, G.G., Patrick, E.L., Raaen, E., Magee, B.A., 2009. Analysis of Titan's neutral upper atmosphere from Cassini Ion Neutral Mass Spectrometer measurements. Icarus 200, 581–615. https://doi.org/10.1016/j.icarus.2008.12.005.

De Kok, R.J., Teanby, N.A., Maltagliati, L., Irwin, P.G.J., Vinatier, S., 2014. HCN ice in Titan's high-altitude southern polar cloud. Nature 514, 65–67. https://doi.org/10.1038/nature13789.

Dinelli, B.M., Puertas, M.L., Fabiano, F., Adriani, A., Moriconi, M.L., Funke, B., García-Comas, M., Oliva, F., D'Aversa, E., Filacchione, G., 2019. Climatology of CH$_4$, HCN and C$_2$H$_2$ in Titan's upper atmosphere from Cassini/VIMS observations. Icarus 331, 83–97. https://doi.org/10.1016/j.icarus.2019.04.026.

Dobrijevic, M., Loison, J.C., Hickson, K.M., Gronoff, G., 2016. 1D-coupled photochemical model of neutrals, cations and anions in the atmosphere of Titan. Icarus 268, 313–339. https://doi.org/10.1016/j.icarus.2015.12.045.

Flasar, F.M., Achterberg, R.K., Conrath, B.J., Gierasch, P.J., Kunde, V.G., Nixon, C.A., Bjoraker, G.L., Jennings, D.E., Romani, P.N., Simon-Miller, A.A., Bézard, B., Coustenis, A., Irwin, P.G.J., Teanby, N.A., Brasunas, J.C., Pearl, J.C., Segura, M.E., Carlson, R.C., Mamoutkine, A., Schinder, P.J., Barucci, A., Courtin, R., Fouchet, T., Gautier, D., Lellouch, E., Marten, A., Prangé, R., Vinatier, S., Strobel, D.F., Calcutt, S.B., Read, P.L., Taylor, F.W., Bowles, N., Samuelson, R.E., Orton, G.S., Spilker, L.J., Owen, T.C., Spencer, J.R., Showalter, M.R., Ferrari, C., Abbas, M.M., Raulin, F., Edgington, S., Ade, P., Wishnow, E.H., 2005. Titan's atmospheric temperatures, winds, and composition. Science 308, 975–979. https://doi.org/10.1126/science.1111150 (80-.).

Flasar, F.M., Kunde, V.G., Abbas, M.M., Achterberg, R.K., Ade, P., Barucci, A., Bézard, B., Bjoraker, G.L., Brasunas, J.C., Calcutt, S.B., Carlson, R.C., Césarsky, C.J., Conrath, B.J., Coradini, A., Courtin, R., Coustenis, A., Edberg, S., Edgington, S., Ferrari, C., Fouchet, T., Gautier, D., Gierasch, P.J., Grossman, K., Irwin, P.G.J., Jennings, D.E., Lellouch, E., Mamoutkine, A.A., Marten, A., Meyer, J.P., Nixon, C.A., Orton, G.S., Spilker, L.J., Owen, T.C., Spencer, J.R., Showalter, M.R., Ferrari, C., Abbas, M.M., Raulin, F., Edgington, S., Ade, P., Wishnow, E.H., 2004. Exploring the Saturn system in the thermal infrared: the composite infrared spectrometer. Space Sci. Rev. 115, 169–297. https://doi.org/10.1007/s11214-004-1454-9.

Fulchignoni, M., Ferri, F., Angrilli, F., Ball, A.J., Bar-Nun, A., Barucci, M.A., Bettanini, C., Bianchini, G., Borucki, W., Colombatti, G., Coradini, M., Coustenis, A., Debei, S., Falkner, P., Fanti, G., Flamini, E., Gaborit, V., Grard, R., Hamelin, M., Harri, A.M., Hathi, B., Jernej, I., Leese, M.R., Lehto, A., Stoppato, P.F.L., López-Moreno, J.J., Mäkinen, T., Mcdonnell, J.A.M., Mckay, C.P., Molina-Cuberos, G., Neubauer, F.M., Lo, J.J., Svedhem, H., Tokano, T., Pirronello, V., Rodrigo, R., Saggin, B., Schwingenschuh, K., Simo, z, Zarnecki, J C, Towner, M C, Trautner, R., Withers, P., 2005. In situ measurements of the physical characteristics of Titan's environment. Nature 438, 785–791. https://doi.org/10.1038/nature04314.

Jacquinet-Husson, N., Crepeau, l., Armante, R., Boutammine, C., Chédin, A., Scott, N.A., Crevoisier, C., Capelle, V., Boone, C., Poulet-Croisvier, N., Barbe, A., Campargue, A., Chris Benner, D., Benilan, Y., Bézard, B., Boudon, V., Brown, L.R., Coudert, L.H., Coustenis, A., Dana, V., Devi, V.M., Fally, S., Fayt, A., Flaud, J.M., Goldman, A., Herman, M., Harris, G.J., Jacquemart, D., Jolly, A., Kleiner, I., Kleinböhl, A., Kwabia-Tchana, F., Lavrentieva, N., Lacome, N., Xu, Li-Hong, Lyulin, O.M., Mandin, J.-Y., Maki, A., Mikhailenko, S.N., Miller, C.E., Mishina, T., Moazzen-Ahmadi, N., Müller, H.S.P., Nikitin, Andrei V., Orphal, J., Perevalov, V.I., Perrin, A., Petkie, D.T., Predoi-Cross, A., Rinsland, C.P., Remedios, J.J., Rotger, M., Smith, Mary

Ann H., Sung, Keeyoon, Tashkun, S.A., Tennyson, Jonathan, Toth, R.A., Vandaele, A.C., Vander Auwera, J., 2011. The 2009 edition of the GEISA spectroscopic database. J. Quant. Spectrosc. Radiat. Transf. 112, 2395–2445. https://doi.org/10.1016/j.jqsrt.2011.06.004.

Jennings, D.E., Anderson, C.M., Samuelson, R.E., Flasar, F.M., Nixon, C.A., Bjoraker, G.L., Romani, P.N., Achterberg, R.K., Cottini, V., Hesman, B.E., Kunde, V.G., Carlson, R.C., De Kok, R., Coustenis, A., Vinatier, S., Bampasidis, G., Teanby, N.A., Calcutt, S.B., 2012. First observation in the south of Titan's far-infrared 220 cm^{-1} cloud. Astrophys. J. Lett. 761, L15. https://doi.org/10.1088/2041-8205/761/1/L15.

Jennings, D.E., Flasar, F.M., Kunde, V.G., Nixon, C.A., Segura, M.E., Romani, P.N., Gorius, N., Albright, S.A., Brasunas, J.C., Carlson, R.C., Mamoutkine, A.A., Guandique, E.A., Kaelberer, M.S., Aslam, S., Achterberg, R.K., Bjoraker, G.L., Anderson, C.M., Cottini, V., Pearl, J.C., Smith, M.D., Hesman, B., Barney, R.D., Calcutt, S., Vellacott, T.J., Spilker, L.J., Edgington, S.G., Brooks, S.M., Ade, P.A.R., Schinder, P.J., Coustenis, A., Courtin, R., Michel, G., Fettig, R.K., Pilorz, S., Ferrari, C., 2017. Composite infrared spectrometer (CIRS) on Cassini. Appl. Opt. 56, 5274–5294. https://doi.org/10.1364/AO.56.005274.

Koskinen, T.T., Yelle, R.V., Snowden, D.S., Lavvas, P., Sandel, B.R., Capalbo, F.J., Benilan, Y., West, R.A., 2011. The mesosphere and lower thermosphere of Titan revealed by Cassini/UVIS stellar occultations. Icarus 216, 507–534. https://doi.org/10.1016/j.icarus.2011.09.022.

Krasnopolsky, V.A., 2012. Titan's photochemical model: further update, oxygen species, and comparison with Triton and Pluto. Planet. Space Sci. 73, 318–326. https://doi.org/10.1016/j.pss.2012.08.013.

Krasnopolsky, V.A., 2014. Chemical composition of Titan's atmosphere and ionosphere: observations and the photochemical model. Icarus 236, 83–91. https://doi.org/10.1016/j.icarus.2014.03.041.

Kunde, V.G., Ade, P.A.R., Barney, R.D., Bergman, D., Bonnal, J.F., Borelli, R., Boyd, D., Brasunas, J.C., Brown, G.V., Calcutt, S.B., Carroll, F., Courtin, R., Cretolle, J.B., Crooke, J.A., Davis, M.A., Edberg, S., Fettig, R.K., Flasar, F.M., Glenar, D.A., Graham, S., Hagopian, J.G., Hakun, C.F., Hayes, P.A., Herath, L., Horn, L., Jennings, D.E., Karpati, G., Kellebenz, C., Lakew, B., Lindsay, J., Lohr, J., Lyons, J.J., Martineau, R.J., Martino, A.J., Matsumura, M., McCloskey, J., Melak, T., Michel, G., Morrell, A., Mosier, C., Pack, L.G., Plants, M., Robinson, D., Rodriguez, L., Romani, P.N., Schaefer, B., Schmidt, S.M., Trujillo, C., Vellacott, T.J., Wagner, K., Yun, D., 1996. Cassini infrared Fourier spectroscopic investigation. Proc. SPIE 2803, 162–177. https://doi.org/10.1117/12.253416.

Lavvas, P., Yelle, R.V., Griffith, C.A., 2010. Titan's vertical aerosol structure at the Huygens landing site: constraints on particle size, density, charge, and refractive index. Icarus 210, 832–842. https://doi.org/10.1016/j.icarus.2010.07.025.

Lebonnois, S., Burgalat, J., Rannou, P., Charnay, B., 2012. Titan global climate model: a new 3-dimensional version of the IPSL Titan GCM. Icarus 218, 707–722. https://doi.org/10.1016/j.icarus.2011.11.032.

Lebonnois, S., Toublanc, D., Hourdin, F., Rannou, P., 2001. Seasonal variations of Titan's atmospheric composition. Icarus 152, 384–406. https://doi.org/10.1006/icar.2001.6632.

Lellouch, E., Bézard, B., Flasar, F.M., Vinatier, S., Achterberg, R.K., Nixon, C.A., Bjoraker, G.L., Gorius, N., 2014. The distribution of methane in Titan's stratosphere from Cassini/CIRS observations. Icarus 231, 323–337. https://doi.org/10.1016/j.icarus.2013.12.016.

Loison, J.C., Hébrard, E., Dobrijevic, M., Hickson, K.M., Caralp, F., Hue, V., Gronoff, G., Venot, O., Bénilan, Y., 2015. The neutral photochemistry of nitriles, amines and imines in the atmosphere of Titan. Icarus 247, 218–247. https://doi.org/10.1016/j.icarus.2014.09.039.

Lora, J.M., Lunine, J.I., Russell, J.L., 2015. GCM simulations of Titan's middle and lower atmosphere and comparison to observations. Icarus 250, 516–528. https://doi.org/10.1016/j.icarus.2014.12.030.

Magee, B.A., Waite, J.H., Mandt, K.E., Westlake, J., Bell, J., Gell, D.A., 2009. INMS-derived composition of Titan's upper atmosphere: analysis methods and model comparison. Planet. Space Sci. 57, 1895–1916. https://doi.org/10.1016/j.pss.2009.06.016.

Newman, C.E., Lee, C., Lian, Y., Richardson, M.I., Toigo, A.D., 2011. Stratospheric superrotation in the TitanWRF model. Icarus 213, 636–654. https://doi.org/10.1016/j.icarus.2011.03.025.

Niemann, H.B., Atreya, S.K., Demick, J.E., Gautier, D., Haberman, J.A., Harpold, D.N., Kasprzak, W.T., Lunine, J.I., Owen, T.C., Raulin, F., 2010. Composition of Titan's lower atmosphere and simple surface volatiles as measured by the Cassini-Huygens probe gas chromatograph mass spectrometer experiment. J. Geophys. Res. 115, E12006. https://doi.org/10.1029/2010JE003659.

Nixon, C.A., Achterberg, R.K., Teanby, N.A., Irwin, P.G.J., Flaud, J.M., Kleiner, I., Dehayem-Kamadjeu, A., Brown, L.R., Sams, R.L., Bézard, B., Coustenis, A., Ansty, T.M., Mamoutkine, A., Vinatier, S., Bjoraker, G.L., Jennings, D.E., Romani, P.N., Flasar, F.M., 2010. Upper limits for undetected trace species in the stratosphere of Titan. Faraday Discuss. 147, 65–81. https://doi.org/10.1039/c003771k.

Nixon, C.A., Ansty, T.M., Lombardo, N.A., Achterberg, R.K., Bjoraker, G.L., Flasar, F.M., Annex, A., Rice, M., 2019. Cassini Composite Infrared Spectrometer (CIRS) observations of Titan 2004-2017. Astrophys. J. Suppl. Ser.

Peralta, J., Imamura, T., Read, P.L., Luz, D., Piccialli, A., López-Valverde, M.A., 2014a. Analytical solution for waves in planets with atmospheric superrotation. I. Acoustic and inertia-gravity waves. Astrophys. J. Suppl. Ser. 213, 17. https://doi.org/10.1088/0067-0049/213/1/17.

Peralta, J., Imamura, T., Read, P.L., Luz, D., Piccialli, A., López-Valverde, M.A., 2014b. Analytical solution for waves in planets with atmospheric superrotation. II. Lamb, surface, and centrifugal waves. Astrophys. J. Suppl. Ser. 213 https://doi.org/10.1088/0067-0049/213/1/18, 18.

Sung, K., Toon, G.C., Mantz, A.W., Smith, M.A.H., 2013. FT-IR measurements of cold C_3H_8 cross sections at 7–15 μm for Titan atmosphere. Icarus 226, 1499–1513. https://doi.org/10.1016/j.icarus.2013.07.028.

Sylvestre, M., Teanby, N.A., Vinatier, S., Lebonnois, S., Irwin, P.G.J., 2018. Seasonal evolution of C_2N_2, C_3H_4, and C_4H_2 abundances in Titan's lower stratosphere. Astron. Astrophys. 609, A64. https://doi.org/10.1051/0004-6361/201630255.

Teanby, N.A., Bézard, B., Vinatier, S., Sylvestre, M., Nixon, C.A., Irwin, P.G.J., De Kok, R. J., Calcutt, S.B., Flasar, F.M., 2017. The formation and evolution of Titan's winter polar vortex. Nat. Commun. 8, 1586. https://doi.org/10.1038/s41467-017-01839-z.

Teanby, N.A., Irwin, P.G.J., Nixon, C.A., De Kok, R.J., Vinatier, S., Coustenis, A., Sefton-Nash, E., Calcutt, S.B., Flasar, F.M., 2012. Active upper-atmosphere chemistry and dynamics from polar circulation reversal on Titan. Nature 491, 732–735. https://doi.org/10.1038/nature11611.

Teanby, N.A., Sylvestre, M., Sharkey, J., Nixon, C.A., Vinatier, S., Irwin, P.G.J., 2019. Seasonal evolution of Titan's stratosphere during the Cassini mission. Geophys. Res. Lett. 46, 3079–3089. https://doi.org/10.1029/2018gl081401.

Thelen, A.E., Nixon, C.A., Chanover, N.J., Cordiner, M.A., Molter, E.M., Teanby, N.A., Irwin, P.G.J., Serigano, J., Charnley, S.B., 2019. Abundance measurements of Titan's stratospheric HCN, HC_3N, C_3H_4, and CH_3CN from ALMA observations. Icarus 319, 417–432. https://doi.org/10.1016/j.icarus.2018.09.023.

Tokano, T., 2013. Wind-induced equatorial bulge in Venus and Titan general circulation models: implication for the simulation of superrotation. Geophys. Res. Lett. 40, 4538–4543. https://doi.org/10.1002/grl.50841.

Vatant d'Ollone, J., Lebonnois, S., Burgalat, J., 2018. Seasonal variations in Titan's stratosphere polar regions addressed with a Global Climate Model. In: EPSC Abstr., pp. EPSC2018–1034.

Vinatier, S., Bézard, B., De Kok, R.J., Anderson, C.M., Samuelson, R.E., Nixon, C.A., Mamoutkine, A., Carlson, R.C., Jennings, D.E., Guandique, E.A., Bjoraker, G.L., Flasar, F.M., Kunde, V.G., 2010a. Analysis of Cassini/CIRS limb spectra of Titan acquired during the nominal mission I. Hydrocarbons, nitriles and CO_2 vertical mixing ratio profiles. Icarus 205, 559–570. https://doi.org/10.1016/j.icarus.2009.08.013.

Vinatier, S., Bézard, B., De Kok, R.J., Anderson, C.M., Samuelson, R.E., Nixon, C.A., Mamoutkine, A., Carlson, R.C., Jennings, D.E., Guandique, E.A., Bjoraker, G.L., Flasar, F.M., Kunde, V.G., 2010b. Analysis of Cassini/CIRS limb spectra of Titan acquired during the nominal mission II: aerosol extinction profiles in the 600–1420 cm^{-1} spectral range. Icarus 210, 852–866. https://doi.org/10.1016/j.icarus.2010.06.024.

Vinatier, S., Bézard, B., Lebonnois, S., Teanby, N.A., Achterberg, R.K., Gorius, N., Mamoutkine, A., Guandique, E., Jolly, A., Jennings, D.E., Flasar, F.M., 2015. Seasonal variations in Titan's middle atmosphere during the northern spring derived from Cassini/CIRS observations. Icarus 250, 95–115. https://doi.org/10.1016/j.icarus.2014.11.019.

Vinatier, S., Fouchet, T., Teanby, N.A., De Kok, R.J., Irwin, P.G.J., Conrath, B.J., Nixon, C.A., Romani, P.N., Flasar, F.M., Coustenis, A., 2007. Vertical abundance profiles of hydrocarbons in Titan's atmosphere at 15°S and 80°N retrieved from Cassini/CIRS spectra. Icarus 188, 120–138. https://doi.org/10.1016/j.icarus.2006.10.031.

Vinatier, S., Rannou, P., Anderson, C.M., Bézard, B., De Kok, R.J., Samuelson, R.E., 2012. Optical constants of Titan's stratospheric aerosols in the 70–1500 cm^{-1} spectral range constrained by Cassini/CIRS observations. Icarus 219, 5–12. https://doi.org/10.1016/j.icarus.2012.02.009.

Vinatier, S., Schmitt, B., Bézard, B., Rannou, P., Dauphin, C., De Kok, R.J., Jennings, D.E., Flasar, F.M., 2018. Study of Titan's fall southern stratospheric polar cloud composition with Cassini/CIRS: detection of benzene ice. Icarus 310, 89–104. https://doi.org/10.1016/j.icarus.2017.12.040.

Vuitton, V., Yelle, R.V., Klippenstein, S.J., Hörst, S.M., Lavvas, P., 2019. Simulating the density of organic species in the atmosphere of Titan with a coupled ion-neutral photochemical model. Icarus 324, 120–197. https://doi.org/10.1016/j.icarus.2018.06.013.

West, R.A., Del Genio, A.D., Barbara, J.M., Toledo, D., Lavvas, P., Rannou, P., Turtle, E. P., Perry, J., 2016. Cassini imaging science subsystem observations of Titan's south polar cloud. Icarus 270, 399–408. https://doi.org/10.1016/j.icarus.2014.11.038.